

Two-Mode Squeezing and Conservation of Optical Angular Momentum
via Four-Wave Mixing in Rubidium

A thesis submitted in partial fulfillment of the requirement
for the degree of Bachelor of Science in Physics from
The College of William and Mary


by

Nathan Super

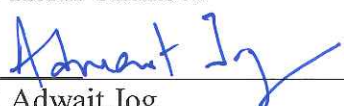
Accepted for Honors



Prof. Irina Novikova, Advisor



Prof. Keith Griffioen



Prof. Adwait Jog

Williamsburg, VA
May 4, 2018

Contents

Acknowledgments	iii
List of Figures	viii
Abstract	ix
1 Introduction	1
1.1 Motivation	1
1.2 Squeezing	3
1.2.1 Single Mode Squeezing	3
1.2.2 Two-Mode Squeezing	6
1.3 Four-Wave Mixing	9
1.3.1 Qualitative Description	9
1.3.2 Classical Description of FWM	11
1.3.3 Quantum Description of FWM	12
1.3.4 Optical Angular Momentum Conservation	16
2 Experimental Technique	20
2.1 Setup	21
2.2 Parameter Optimization	22
2.3 Noise Measurements	23

2.4	OAM Experiment	24
3	Intensity Squeezing Optimization	27
3.1	Preliminary Results	27
3.2	Shot Noise Recalibration and Results	28
3.3	Power Dependence of Squeezing	31
4	OAM Results	33
4.1	Input Probe Beam Carrying a Vortex	33
4.2	Pump Beam Carrying a Vortex	35
4.3	Probe and Pump with Same Charge Vortex	36
4.4	Probe and Pump with Opposite Charge Vortex	37
5	Conclusions	47
5.1	Future Plans	48
5.1.1	Bell States	48
5.1.2	Polarization Entanglement	49

Acknowledgments

I'd like to thank Irina Novikova for her tireless advice and guidance. I can always rely on her to push me to better myself, whether in experimental physics or in daily life. I would also like to thank Nikunj Prajapati for making days in lab infinitely more enjoyable, and for spurring on the experiment when it had stagnated. This work is supported by National Science Foundation under grant No. PHY-308281.

List of Figures

1.1	Example phasor, with amplitude A , phase ϕ , and quadratures X and Y . [2]	4
1.2	Phasor representation of a coherent state. [2]	6
1.3	(a) Coherent state, (b) Phase-squeezed state, (c) Amplitude-squeezed state. [2].	7
1.4	(a) Uncorrelated fields, with the noise of a coherent field represented by the dashed ring. (b) Amplitude squeezed fields, showing the decrease in \hat{X}_- and \hat{Y}_+ and the increase in \hat{X}_+ and \hat{Y}_- . [2]	8
1.5	FWM process in terms of the energy levels of the ^{85}Rb system. ω_0 is the pump frequency, ω_c is the conjugate frequency, ω_p is the probe frequency, ω_{HF} is the hyperfine splitting of 3036 MHz, Δ_1 is the pump detuning, $\Delta_2 = \Delta_1 + \omega_{HF}$, δ is the two-photon detuning.	9
1.6	Graphical representation of FWM process. The pump and probe combine at a small angle before the Rb cell, and probe, pump, and Stokes emerge, probe and pump symmetric around the pump.	10
1.7	$\text{sinc}(x)$	16
1.8	LG Modes. [10]	18
2.1	Schematic for the experimental setup of this project.	20
2.2	Closer look at the probe setup.	21

2.3	Closer look at cell and detection setup.	22
2.4	Schematic with the diffraction grating in the probe path and the phase mask in the pump path.	25
2.5	Top row: charge 1, with and without tilt; middle row: charge 2, with and without tilt; bottom row: charge 3, with and without tilt. [13] . .	26
2.6	Left: LG_{01} mode without interference; right: the same mode interfered with a plane-wave. [14]	26
3.1	Differential noise between Stokes and probe in black, and the quantum shot noise limit in red. We see as much as -4.5 dB of squeezing. . . .	28
3.2	Shot noise calibrations.	29
3.3	Squeezing vs detuning with cell temperature of 92 °C. The left axis corresponds to the squeezing level of each measurement, and the right axis corresponds to the signal strength of probe and Stokes of each measurement. The x-axis corresponds to the two-photon detuning, or how far the probe is detuned from the pump frequency.	30
3.4	Squeezing vs detuning with cell temperature of 96 °C. The left axis corresponds to the squeezing level of each measurement, and the right axis corresponds to the signal strength of probe and Stokes of each measurement. The x-axis corresponds to the two-photon detuning, or how far the probe is detuned from the pump frequency.	30
3.5	Same as Fig. 3.3, except the cell temperature was 100 °C. The x-axis corresponds to the two-photon detuning, or how far the probe is detuned from the pump frequency.	31

3.6	Same as Fig. 3.3, except the cell temperature was 110 °C. The x-axis is defined as the two-photon detuning as defined in Fig. 3.3 minus the hyperfine splitting frequency of 3035 MHz.	31
3.7	Best squeezing vs detuning results (pump power of 350 mW, T = 100 °C). The axes are defined the same as in Fig. 3.3.	32
3.8	Best squeezing so far. The blue line is the raw data, black line is SNL for input power, red line is smoothed differential noise data.	32
3.9	Squeezing vs detuning with 450 mW pump power. The axes are defined the same as in Fig. 3.3. The cell temperature was 96 °C.	32
3.10	Same as Fig. 3.9, except the pump power was 390 mW.	32
3.11	Same as Fig. 3.9, except the pump power was 295 mW.	32
3.12	Same as Fig. 3.9, except the pump power was 175 mW.	32
4.1	Beam profiles of probe and Stokes at -22 MHz for vortex in probe input.	34
4.2	Beam profiles of probe and Stokes at -12 MHz for vortex in probe input.	34
4.3	Beam profiles of probe and Stokes at -6 MHz for vortex in probe input.	34
4.4	Squeezing vs detuning with vortex of $m = +1$ on the probe input. The left axis corresponds to the squeezing level for each measurements, and the right axis corresponds to the signal strength of the probe and Stokes for each measurement. The x-axis is the two-photon detuning minus the hyperfine splitting frequency of 3035 MHz.	35
4.5	Beam profiles of Stokes, pump, and probe at -85 MHz for vortex in pump input. Stokes on left, pump in center, probe on right. Interfered with plane-waves on top, without interference on bottom.	38

4.6	Beam profiles of Stokes, pump, and probe at -55 MHz for vortex in pump input. Stokes on left, pump in center, probe on right. Interfered with plane-waves on top, without interference on bottom.	38
4.7	Beam profiles of Stokes, pump, and probe at -25 MHz for vortex in pump input. Stokes on left, pump in center, probe on right. Interfered with plane-waves on top, without interference on bottom.	38
4.8	Beam profiles of Stokes, pump, and probe at -5 MHz for vortex in pump input. Stokes on left, pump in center, probe on right. Interfered with plane-waves on top, without interference on bottom.	38
4.9	Same as Fig. 4.4, but with vortex of $m = -1$ on the pump input and no vortex on the probe input.	39
4.10	Same as Fig. 4.4, but with vortex of $m = -1$ on both input fields. . .	39
4.11	Beam profiles of probe and Stokes with (left) and without (right) interference at -15 MHz for same charge in pump and probe input. . . .	40
4.12	Beam profiles of probe and Stokes with (left) and without (right) interference at -6 MHz for same charge in pump and probe input. The Stokes is the beam on the left in its images.	41
4.13	Beam profiles of probe and Stokes with (left) and without (right) interference at -3 MHz for same charge in pump and probe input. . . .	42
4.14	Same as Fig. 4.4, but with vortex of $m = -1$ on probe input field, $m = +1$ on pump input field.	43
4.15	Beam profiles of probe and Stokes with (left) and without (right) interference at -14 MHz for opposite in pump and probe input. The Stokes field is on the left of its images.	44
4.16	Beam profiles of probe and Stokes with (left) and without (right) interference at -7 MHz for opposite charge in pump and probe input. .	45

4.17 Beam profiles of probe and Stokes with (left) and without (right) interference at -1 MHz for opposite charge in pump and probe input. . .	46
--	----

Abstract

The goal of the project is to produce a pair of intensity-squeezed light fields using Four-Wave Mixing (FWM) in hot Rubidium vapor. In this process, interaction of atoms with near-resonant strong control optical field results in strong amplification of a weak probe optical field and in generation of a quantum correlated conjugate Stokes optical field. In order to establish the quantum correlation between the Stokes and probe fields, we measured the differential intensity noise between the Stokes and probe fields. If the noise falls below the quantum noise limit, then two-mode intensity squeezing has been achieved, as a first step toward realization of the polarization Bell states. We also examine the conservation of orbital angular momentum (OAM) in the FWM process with OAM-bearing input fields.

Chapter 1

Introduction

1.1 Motivation

In many experimental systems, it is important to have the highest measurement sensitivity possible. A popular technique for increasing sensitivity in noisy optical systems is to split the input field in two before the experiment, send one branch through the experiment, and subtract the other from the signal-bearing field. For classical electromagnetic fields, this method leads to the complete erasure of the noise in the field, and resolution of the experimental data limited only by the measuring device. Unfortunately for us, we do not live in an optical world that can be accurately described by classical electrodynamics, and our EM fields carry intrinsic, independently propagating noise that cannot be removed by a simple subtraction method. This intrinsic EM noise, known as shot noise (SNL refers to the shot noise limit), limits the best resolution achievable with optical measurements. For most experiments, this level of noise is far lower than other technical noises in their systems, and so this is a limit they never run up against. But for certain high resolution experiments, such as LIGO's gravitational wave detection system and the fields of optical imaging and photolithography, the quantum noise limit is a fundamental roadblock to further progress.

The quantum nature of light leads to the noise problem I described above, but it also provides a mechanism to circumvent this problem. Through nonlinear processes, we can produce squeezed light, which reduces noise in either amplitude or phase, and correspondingly produces higher noise in the other, due to a Heisenberg uncertainty relation between these quantities. Two-mode squeezing is a similar concept that occurs when the fluctuations in two fields are correlated. Two-mode amplitude squeezed light can be used in a differential measurement scheme similar to the ideal classical case, and noise levels below shot noise can be achieved. One such nonlinear process that can produce two-mode amplitude squeezed light is Four-Wave Mixing (FWM). I will go into more detail on this later, but this is a process where two input fields lead to three output fields, two of which are amplitude squeezed relative to each other.

Another aspect of this experiment involves the conservation of optical angular momentum in this FWM setup. This is important for quantum communication and imaging techniques, as it provides additional information storage capacity. Any field of arbitrary spatial structure can be thought of as a sum of plain-waves. Since these plain-waves are basis modes, they are orthogonal and are squeezed independently. Each of these modes can be used to store quantum information. For the FWM setup, there is a bandwidth of k -vectors that has gain and the resulting squeezing. We can also relate these spatial modes to their optical orbital angular momenta. We investigate the conservation of the optical angular momentum (OAM) by imposing OAM on our input beams and observing the resulting spatial structure of our output beams.

The long-term goals of this experiment are for applications with polarization entanglement. Light entanglement is a feature of quantum mechanics that is entirely impossible in a classical understanding of the universe. In essence, if the two fields are entangled, it means that a measurement on one of the fields absolutely determines

the state of the other, without measurement and without interaction. To put this in quantum mechanical terms, the two fields have states that are superimposed in a way that makes independent characterization impossible. This is represented generically in Eq. 1.1. The measurement of one field collapses the combined state superimposition, determining the state of the other field. This phenomenon provides a way to realize qubits, the quantum analog to the bits of classical computing, as well as possibilities in quantum imaging, communication, and improved sensor technology. In this particular experiment, we are working on entangling polarization and frequency modes so that we can perform the classic Bell state measurements.

$$|\Psi\rangle_{1,2} = \frac{1}{\sqrt{2}}(|\Psi_1\rangle \pm |\Psi_2\rangle) \quad (1.1)$$

1.2 Squeezing

1.2.1 Single Mode Squeezing

A classical field can be described as a phasor, a vector that represents the field's amplitude as its length and its phase as an angle. The axes of this vector are known as quadratures, a phrase that will be brought up throughout this thesis. An example is shown in Fig. 1.1.

We can describe an electric field of a single photon as

$$E(t) = 2\mathcal{E}_0(X\cos(\omega t) + Y\sin(\omega t)) \quad (1.2)$$

where $\mathcal{E}_0 = \sqrt{\hbar\omega/2\epsilon_0 V}$ is the electric field amplitude, ω is the angular frequency, and V is the active volume of the field[1]. For quantum mechanical description of EM fields, the X, Y are replaced with the operators \hat{X}, \hat{Y}

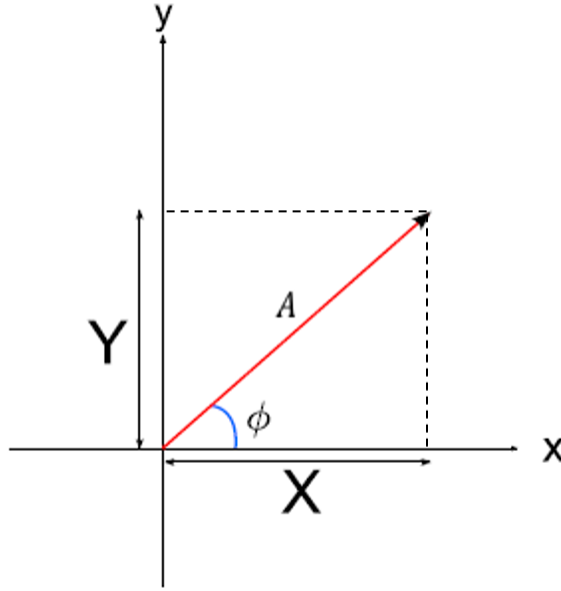


Figure 1.1: Example phasor, with amplitude A , phase ϕ , and quadratures X and Y . [2]

$$\hat{X} = \frac{\hat{a} + \hat{a}^\dagger}{2} \quad (1.3a)$$

$$\hat{Y} = \frac{\hat{a} - \hat{a}^\dagger}{2i} \quad (1.3b)$$

where \hat{a}, \hat{a}^\dagger are the annihilation and creation operators, respectively. Acting on the Fock states[3] with given photon number n , $|n\rangle$, these operators lower and raise the number of photons in the field as such

$$\hat{a} |n\rangle = \sqrt{n} |n-1\rangle \quad (1.4a)$$

$$\hat{a}^\dagger |n\rangle = \sqrt{n+1} |n+1\rangle \quad (1.4b)$$

$$\hat{n} |n\rangle = \hat{a}^\dagger \hat{a} |n\rangle = n |n\rangle \quad (1.4c)$$

where \hat{n} is the number operator that retrieves the current number of photons in the field.

\hat{X} and \hat{Y} have a commutation relation[2]

$$[\hat{X}, \hat{Y}] = \frac{i}{2} \quad (1.5)$$

that leads to the following uncertainty relation

$$\langle(\Delta\hat{X})^2\rangle\langle(\Delta\hat{Y})^2\rangle \geq \frac{1}{16} \quad (1.6)$$

When the minimum uncertainty is evenly shared between the two quadratures, i.e.,

$$\Delta\hat{X} = \Delta\hat{Y} = \frac{1}{2} \quad (1.7)$$

we say that we are dealing with a coherent state, $|\alpha\rangle$. These coherent states can be represented in the Fock basis as such

$$|\alpha\rangle = e^{-|\alpha|^2/2} \sum_{n=1}^{\infty} \frac{\alpha^n}{\sqrt{n!}} |n\rangle \quad (1.8)$$

These states are most closely related to the representations of classical fields with the lowest possible noise, i.e. at the quantum noise limit (QNL). It is worth noting that

$$\hat{a}|\alpha\rangle = \alpha|\alpha\rangle \quad (1.9)$$

Their uncertainty appears as a round ball on a phasor diagram, as shown in Fig. 1.2.

Like Turnbull[2], we will refer to the uncertainty in \hat{X} as amplitude uncertainty and the uncertainty in \hat{Y} as phase uncertainty, since we can rotate phasors with a simple change of basis such that our phasor lies on the X axis.

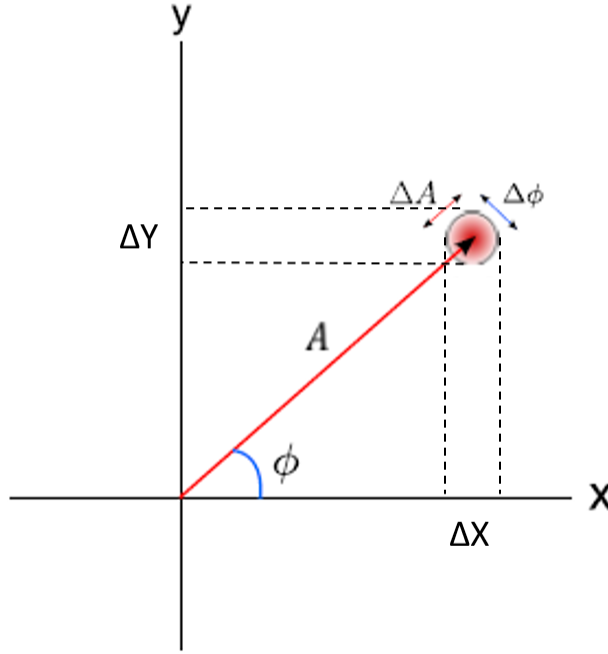


Figure 1.2: Phasor representation of a coherent state. [2]

I have spent this time introducing a framework through which squeezing can be understood, but I have yet to address the concept itself. A squeezed light state is one in which the uncertainty is unevenly distributed between X and Y , such that Eq. 1.7 is satisfied, i.e. $\Delta\hat{X} > \frac{1}{2}, \Delta\hat{Y} < \frac{1}{2}$ or vice versa. These conditions results in a phasor where the uncertainty stretches from a ball into an ellipse along the Y and X axes respectively, as shown in Fig. 1.3.

Phase-squeezed light can be measured with greater precision in its phase and less precision in its amplitude, and amplitude-squeezed light can be measured with greater precision in its amplitude and less precision in its phase.

1.2.2 Two-Mode Squeezing

While the previous section is sufficient to understand the generation of single-mode squeezed light, for our purposes, we must deal with two-mode squeezing, in which two optical fields are quantum correlated. Specifically, this will deal with relative intensity

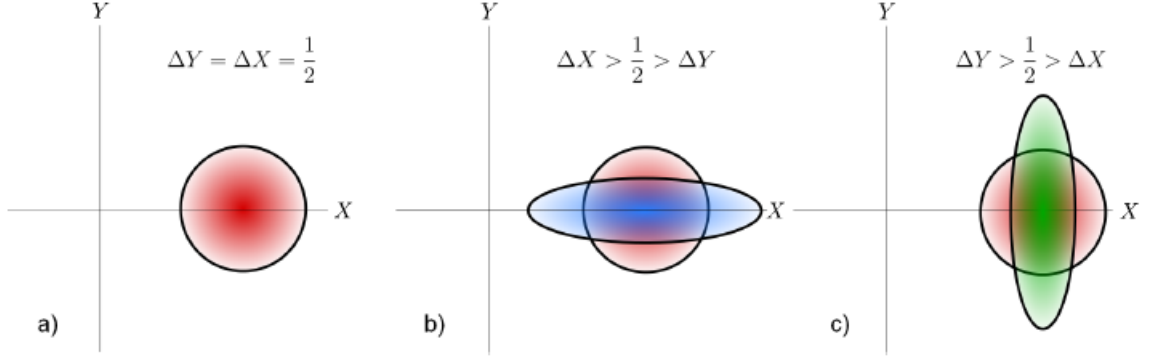


Figure 1.3: (a) Coherent state, (b) Phase-squeezed state, (c) Amplitude-squeezed state. [2].

squeezing, wherein two entangled light fields have correlated amplitude fluctuations.

If we have two EM fields of the same frequency, ω , we can describe them[2] as

$$\hat{E}_1(t) = 2\mathcal{E}_0[\hat{X}_1 \cos \omega t + \hat{Y}_1 \sin \omega t] \quad (1.10a)$$

$$\hat{E}_2(t) = 2\mathcal{E}_0[\hat{X}_2 \cos \omega t + \hat{Y}_2 \sin \omega t] \quad (1.10b)$$

and define the following joint quadrature terms

$$\hat{X}_+ = \frac{1}{\sqrt{2}}(\hat{X}_1 + \hat{X}_2) \quad (1.11a)$$

$$\hat{X}_- = \frac{1}{\sqrt{2}}(\hat{X}_1 - \hat{X}_2) \quad (1.11b)$$

$$\hat{Y}_+ = \frac{1}{\sqrt{2}}(\hat{Y}_1 + \hat{Y}_2) \quad (1.11c)$$

$$\hat{Y}_- = \frac{1}{\sqrt{2}}(\hat{Y}_1 - \hat{Y}_2) \quad (1.11d)$$

As Turnbull derives, we see that the following uncertainty relations hold

$$[\hat{X}_\pm, \hat{Y}_\pm] = \frac{i}{2} \quad (1.12a)$$

$$[\hat{X}_\pm, \hat{Y}_\mp] = 0 \quad (1.12b)$$

which means that we can simultaneously observe squeezing in \hat{X}_+ and \hat{Y}_- or vice versa.

In our case, we deal with relative intensity squeezing, so the squeezed quantities are \hat{X}_- and \hat{Y}_+ . This means that the same temporal fluctuations are present in photon count in E_1 and E_2 . When a differential measurement of the two fields is taken, we will see a reduced noise below the QNL. At the same time, the increased noise in X_+ means that the individual fields will have increased amplitude noise (i.e., gain). This situation is shown in Fig. 1.4.

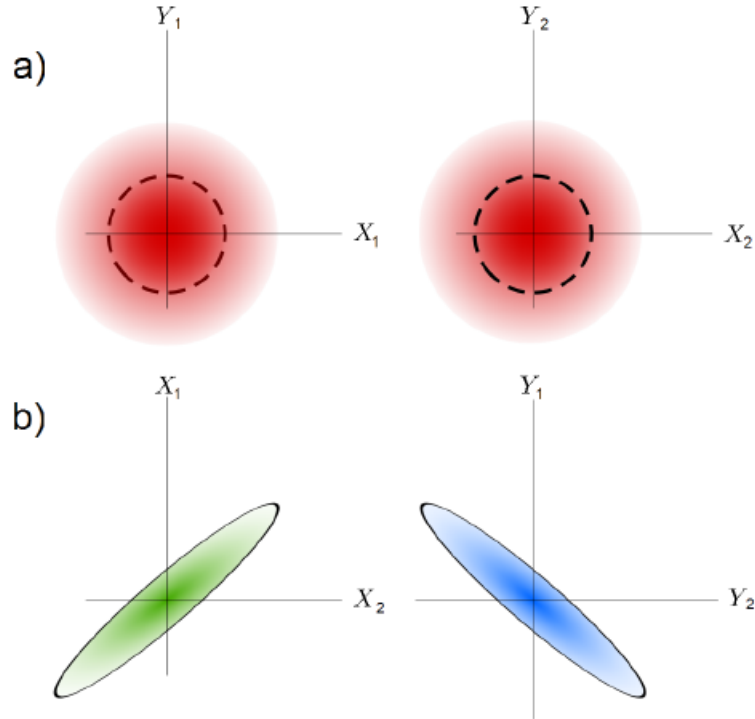


Figure 1.4: (a) Uncorrelated fields, with the noise of a coherent field represented by the dashed ring. (b) Amplitude squeezed fields, showing the decrease in \hat{X}_- and \hat{Y}_+ and the increase in \hat{X}_+ and \hat{Y}_- . [2]

1.3 Four-Wave Mixing

1.3.1 Qualitative Description

In order to entangle the polarizations and frequencies of two fields, we need them to be intensity-correlated. We will be taking advantage of a 3rd-order, non-linear atomic process, Four-Wave Mixing (FWM), in Rubidium in order to obtain these intensity-correlated fields. FWM involves sending a powerful optical field, called the pump or control field, into a Rubidium vapor cell. When a weaker field, called the probe, is sent in, a third field, the Stokes or conjugate field, is generated by Raman scattering of incident photons. The probe and Stokes both experience an intensity gain through this process. A graphical representation of this process is shown in Fig. 1.6, and an energy level diagram in Fig. 1.5 shows that the process is a parametric double-lambda transition.

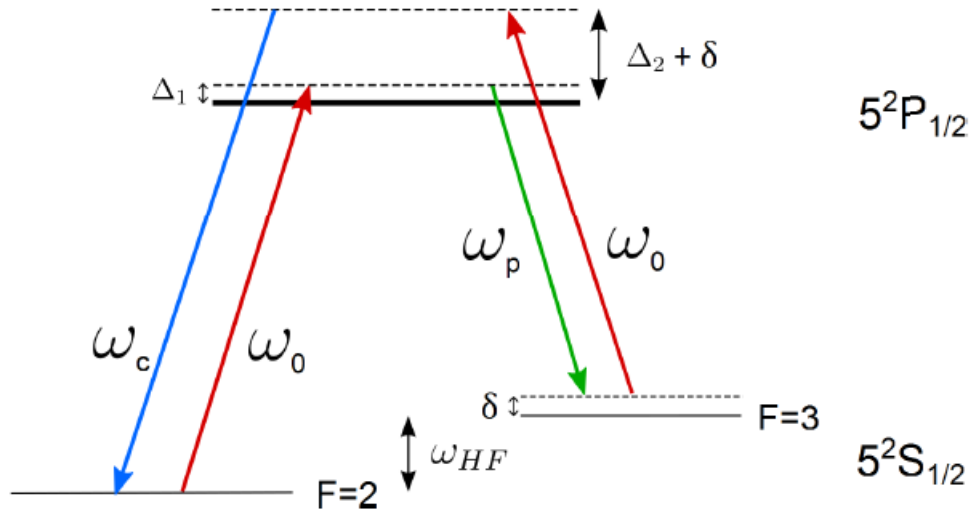


Figure 1.5: FWM process in terms of the energy levels of the ^{85}Rb system. ω_0 is the pump frequency, ω_c is the conjugate frequency, ω_p is the probe frequency, ω_{HF} is the hyperfine splitting of 3036 MHz, Δ_1 is the pump detuning, $\Delta_2 = \Delta_1 + \omega_{HF}$, δ is the two-photon detuning.

$5^2S_{1/2}$ is the ground state, and the $F = 2$ and $F = 3$ are the hyperfine-splitting of

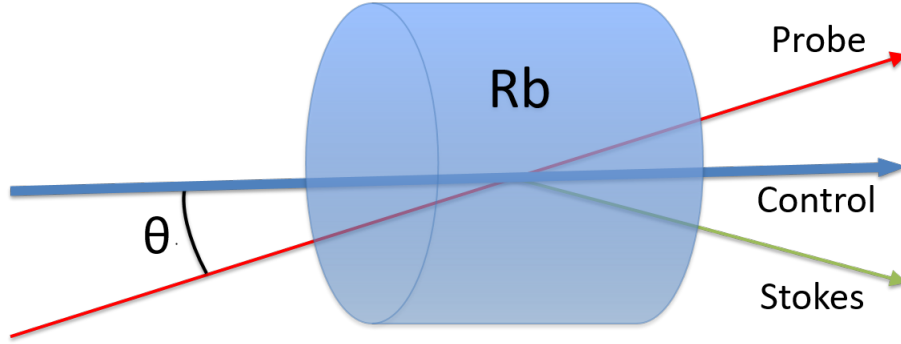


Figure 1.6: Graphical representation of FWM process. The pump and probe combine at a small angle before the Rb cell, and probe, pump, and Stokes emerge, probe and pump symmetric around the pump.

the ground state. $5^2P_{1/2}$ is the first excited state. The control couples the $5^2S_{1/2,F=2}$ to $5^2P_{1/2}$ transition, pumping electrons into the excited state, and the probe couples the $5^2P_{1/2}$ to $5^2S_{1/2,F=3}$ transition, sending electrons down via stimulated emission. The control also couples to a virtual state, detuned from the excited state by approximately one hyperfine splitting energy. Due to Raman scattering, the conjugate Stokes field closes the cycle to the $F = 2$ state. Through this process, two control photons are converted into a Stokes photon and a probe photon. The frequency relations are governed by Eq. 1.13a, and the directional relations (wave-vectors) are governed by Eq. 1.13b, with the 0 subscript referring to the pump, and the c and p corresponding to conjugate (Stokes) and probe.

$$\omega_c = 2\omega_0 - \omega_p \quad (1.13a)$$

$$\Delta\mathbf{k} = 2\mathbf{k}_0 - \mathbf{k}_p - \mathbf{k}_c = 0 \quad (1.13b)$$

Since the nonlinear process leads to generation of probe and Stokes photons simultaneously, the two fields are intensity correlated. This means that fluctuations in the intensities of the fields will be identical. The difference in noise between the two fields is lower than the noise in either individual field, making this system highly effective

in lowering noise. Given a strong enough interaction without much decoherence, it is possible to achieve noise measurements below the QNL, the noise level we would expect from two independent coherent fields of the same intensities

1.3.2 Classical Description of FWM

A more detailed derivation of FWM process and the resultant two-mode squeezing follows, taking inspiration from Turnbull[2] and Jasperse[4]. FWM is a nonlinear optical process, which is driven by nonlinear polarization components. In many materials, polarization has a linear relationship with the electric field

$$P^{(1)}(t) = \epsilon_0 \chi^{(1)} E(t) \quad (1.14a)$$

$$E(t) = \mathcal{E}_0 \sin \omega t \quad (1.14b)$$

$$\nabla^2 E - \frac{1}{c^2} \frac{\partial^2 E}{\partial t^2} = \frac{1}{\epsilon_0 c^2} \frac{\partial^2 P}{\partial t^2} \quad (1.14c)$$

ϵ_0 is the permittivity of free space and $\chi^{(1)}$ is the linear optical susceptibility of the material. Eq. 1.14c is the wave equation for the E field in a medium.

More exactly, polarization can be decomposed in powers of E

$$P(t) = P^{(1)} + P^{(2)} + P^{(3)} + \dots = \epsilon_0 [\chi^{(1)} E(t) + \chi^{(2)} E^2(t) + \chi^{(3)} E^3(t) + \dots] \quad (1.15)$$

where $P^{(n)}$ is the n -th order polarization and $\chi^{(n)}$ is the n -th order optical susceptibility. Rubidium is a $\chi^{(3)}$ medium, which means that the 3rd order polarization is the dominant effect at high powers. Inversion symmetry causes $\chi^{(2)} = 0$. In the process described in the previous section, the 3rd order polarization is as follows[5]

$$P^{(3)}(t) = \sum_{n \in \{0,p,c\}} P(\omega_n) e^{-i\omega_n t} \quad (1.16)$$

with

$$P(\omega_c) = 3\epsilon_0\chi^{(3)}(\omega_c)(E_0)^2 E_p^* \quad (1.17)$$

as one possible permutation. Boyd[5] calculates all the possible permutations of frequencies generated by this scheme, but since the pump is so much stronger than the probe and conjugate, the polarization terms that create the strongest fields are those with $(E_0)^2$ [6]. These terms are [7]

$$P(\omega_p) = \epsilon_0\chi^{(D)}(\omega_p)(\mathcal{E}_0)^2 e^{i\mathbf{k}_p \cdot \mathbf{r}} + \epsilon_0\chi^{(C)}(\omega_p)(\mathcal{E}_0)^2 e^{i(2\mathbf{k}_0 - \mathbf{k}_c) \cdot \mathbf{r}} \quad (1.18a)$$

$$P(\omega_c = 2\omega_0 - \omega_p) = \epsilon_0\chi^{(D)}(\omega_c)(\mathcal{E}_0)^2 e^{i\mathbf{k}_c \cdot \mathbf{r}} + \epsilon_0\chi^{(C)}(\omega_c)(\mathcal{E}_0)^2 e^{i(2\mathbf{k}_0 - \mathbf{k}_p) \cdot \mathbf{r}} \quad (1.18b)$$

with \mathcal{E}_i being the field strength, χ_i being the susceptibility, ω_i being the frequency and \mathbf{k}_i being the wavevector for each field in vacuum. The D superscript for χ is the direct, linear susceptibility, and the C superscript is the cross-coupling susceptibility. If we plug these back into Eq. 1.14c, we will get a series of coupled equations that are solvable for the temporal and spatial behavior of this system. We will see the annihilation of two pump photons and the creation of a probe and a Stokes photon.

1.3.3 Quantum Description of FWM

The interaction Hamiltonian of this system can be expressed as follows[4]

$$\hat{\mathcal{H}} = i\hbar\beta\hat{b}^\dagger\hat{c}\hat{a}^\dagger\hat{c} + h.c. \quad (1.19)$$

where β is the interaction strength, \hat{b}^\dagger and \hat{a}^\dagger are the Stokes and probe creation operators respectively, \hat{c} is the annihilation operator for the pump, and $h.c.$ denotes the Hermitian conjugate of the first term. We will use the undepleted pump approximation, where we assume that the relative strength of the pump is so much higher than

the other fields that the interaction doesn't noticeably deplete the pump's photon count. More specifically

$$\alpha_{pump}(z = 0) \approx \alpha_{pump}(z = L) \rightarrow \frac{d\alpha_{pump}}{dz} \approx 0 \quad (1.20a)$$

$$\hat{\mathcal{H}} = i\hbar\beta\alpha_{pump}^2\hat{b}^\dagger\hat{a}^\dagger + h.c. \quad (1.20b)$$

We can rewrite Eq. 1.20b as follows

$$\hat{\mathcal{H}} = i\hbar\xi\hat{b}^\dagger\hat{a}^\dagger + h.c. \quad (1.21)$$

with ξ representing the overall interaction strength, since we can choose α_{pump} to be real[4]. We can also define the time-evolution operator for this Hamiltonian

$$\hat{U}(t) = e^{\frac{i\hat{\mathcal{H}}t}{\hbar}} = e^{-\xi(\hat{a}\hat{b} - \hat{b}^\dagger\hat{a}^\dagger)t} \quad (1.22)$$

If the process occurs over a timescale τ , we can define the squeezing operator as such

$$\hat{S} = \hat{U}(\tau) = e^{s(\hat{b}^\dagger\hat{a}^\dagger - \hat{a}\hat{b})} \quad (1.23)$$

with $s = \xi\tau$ known as the squeezing parameter[8].

We can also look at the time evolution of the creation and annihilation operators

$$\frac{d\hat{a}}{dt} = \frac{i}{\hbar}[\hat{\mathcal{H}}, \hat{a}] = \xi\hat{b}^\dagger \quad (1.24a)$$

$$\frac{d\hat{b}}{dt} = \frac{i}{\hbar}[\hat{\mathcal{H}}, \hat{b}] = \xi\hat{a}^\dagger \quad (1.24b)$$

Differentiating Eq. 1.24a,1.24b and solving the equations of motion generated there leads to the following time-dependent creation and annihilation operators

$$\hat{a}(t) = \cosh(\xi t)\hat{a}_i + \sinh(\xi t)\hat{b}_i^\dagger \quad (1.25a)$$

$$\hat{b}(t) = \cosh(\xi t)\hat{b}_i + \sinh(\xi t)\hat{a}_i^\dagger \quad (1.25b)$$

where the i subscript denotes the initial fields at $t = 0$. Observing these operators after the interaction, at time τ , leads to the following matrix

$$\begin{pmatrix} \hat{a}(\tau) \\ \hat{b}^\dagger(\tau) \end{pmatrix} = \begin{pmatrix} \cosh s & \sinh s \\ \sinh s & \cosh s \end{pmatrix} \begin{pmatrix} \hat{a}_i \\ \hat{b}_i^\dagger \end{pmatrix} \quad (1.26)$$

From here we can show how the number states of the fields evolve from the interaction. We operate in a regime with a vacuum input for the conjugate, so $\langle \hat{b}^\dagger \hat{b} \rangle(t = 0) = 0$. Calculating the expectation values for $\langle \hat{b}^\dagger \hat{b} \rangle$ and $\langle \hat{a}^\dagger \hat{a} \rangle$ after the interaction can be done by calculating $\langle \alpha_a | \hat{a}^\dagger(\tau) \hat{a}(\tau) | \alpha_a \rangle$ and $\langle \alpha_b | \hat{b}^\dagger(\tau) \hat{b}(\tau) | \alpha_b \rangle$. This yields the following expectation values[4]

$$\langle \hat{N}_a(\tau) \rangle \equiv \langle \hat{a}^\dagger(\tau) \hat{a}(\tau) \rangle = \cosh^2(s) \langle \hat{a}_i^\dagger \hat{a}_i \rangle + \sinh^2(s) \approx G \langle \hat{a}_i^\dagger \hat{a}_i \rangle \quad (1.27a)$$

$$\langle \hat{N}_b(\tau) \rangle \equiv \langle \hat{b}^\dagger(\tau) \hat{b}(\tau) \rangle = \sinh^2(s) \langle \hat{a}_i^\dagger \hat{a}_i \rangle + \sinh^2(s) \approx (G - 1) \langle \hat{a}_i^\dagger \hat{a}_i \rangle \quad (1.27b)$$

$$\langle \hat{N}_a(\tau) + \hat{N}_b(\tau) \rangle = \cosh(2s) \langle \hat{a}_i^\dagger \hat{a}_i \rangle + 2\sinh^2(s) \approx (2G - 1) \langle \hat{a}_i^\dagger \hat{a}_i \rangle \quad (1.27c)$$

$$\langle \hat{N}_a(\tau) - \hat{N}_b(\tau) \rangle = \langle \hat{a}_i^\dagger \hat{a}_i \rangle \quad (1.27d)$$

where $G = \cosh^2(s)$ is our gain factor. It can be shown that the number difference, $\hat{N}_a - \hat{N}_b$, is invariant under the squeezing operator, and so the variance after the interaction can be shown to be the following[4]

$$\text{Var}(\hat{N}_a(\tau) - \hat{N}_b(\tau))_{SQZ} = \text{Var}(\hat{a}_i^\dagger \hat{a}_i - \hat{b}_i^\dagger \hat{b}_i) = \text{Var}(\hat{a}_i^\dagger \hat{a}_i) = \langle \hat{a}_i^\dagger \hat{a}_i \rangle \quad (1.28)$$

For a coherent state (i.e., at the QNL) of the same magnitude, however, we would expect a variance of the following[4]

$$\text{Var}(\hat{N}_a - \hat{N}_b)_{QNL} \equiv \langle \hat{N}_a + \hat{N}_b \rangle \approx (2G - 1) \langle \hat{a}_i^\dagger \hat{a}_i \rangle \quad (1.29)$$

We can then define the degree of squeezing (DS) as

$$DS = \frac{Var(\hat{N}_a - \hat{N}_b)_{SQZ}}{Var(\hat{N}_a - \hat{N}_b)_{QNL}} \approx \frac{\langle \hat{a}_i^\dagger \hat{a}_i \rangle}{(2G - 1)\langle \hat{a}_i^\dagger \hat{a}_i \rangle} = \frac{1}{2G - 1} \quad (1.30)$$

We can look at the logarithmic degree of squeezing, $DS^{(dB)} = 10 \log_{10}(DS)$. Since G comes from s , this means that the stronger the FWM interaction (and consequently the stronger the gain in the probe and the generation in the Stokes), the more negative the $DS^{(dB)}$ and the more the noise is reduced.

We can examine the effect of phase mismatch from the ideal case of Eqs. 1.13a,1.13b by amending the interaction Hamiltonian, Eq. 1.19. We can add a phase term to each creation and annihilation operator to yield the following[4]

$$\begin{aligned} \hat{\mathcal{H}} &\propto (e^{-i\mathbf{k}_c \cdot \mathbf{r} - \omega_c t} \hat{b}^\dagger)(e^{-i\mathbf{k}_0 \cdot \mathbf{r} - \omega_0 t} \hat{c})(e^{-i\mathbf{k}_p \cdot \mathbf{r} - \omega_p t} \hat{a}^\dagger)(e^{-i\mathbf{k}_0 \cdot \mathbf{r} - \omega_0 t} \hat{c}) + h.c. \\ &= [e^{i(2\mathbf{k}_0 - \mathbf{k}_p - \mathbf{k}_c) \cdot \mathbf{r}} e^{2\omega_0 - \omega_p - \omega_c}] \hat{b}^\dagger \hat{c} \hat{a}^\dagger \hat{c} + h.c. \\ &= [e^{i\Delta\mathbf{k} \cdot \mathbf{r} - i\Delta\omega t}] \hat{b}^\dagger \hat{c} \hat{a}^\dagger \hat{c} + h.c. \end{aligned} \quad (1.31)$$

where $\Delta\mathbf{k} = 2\mathbf{k}_0 - \mathbf{k}_p - \mathbf{k}_c$ and $\Delta\omega = 2\omega_0 - \omega_p - \omega_c$ are the wavevector and frequency mismatches from ideal phase matching conditions.

If we integrate Eq. 1.31 in the interaction volume ($\mathcal{V} = l_x l_y l_z$), we find[4]

$$H \propto \left[\chi^{(3)} l_x l_y l_z \text{sinc}\left(\frac{l_x(\Delta\mathbf{k})_x}{2\pi}\right) \text{sinc}\left(\frac{l_y(\Delta\mathbf{k})_y}{2\pi}\right) \text{sinc}\left(\frac{l_z(\Delta\mathbf{k})_z}{2\pi}\right) \right] \hat{b}^\dagger \hat{c} \hat{a}^\dagger \hat{c} + h.c. \quad (1.32)$$

where

$$\text{sinc}(x) = \begin{cases} \frac{\sin(\pi x)}{\pi x} & \text{for } x \neq 0 \\ 1 & \text{for } x = 0 \end{cases}$$

and Fig. 1.7 shows the function.

This shows that the interaction strength of the FWM process is dampened significantly by the \mathbf{k} mismatch, but still yields a valid spatial bandwidth wherein strong

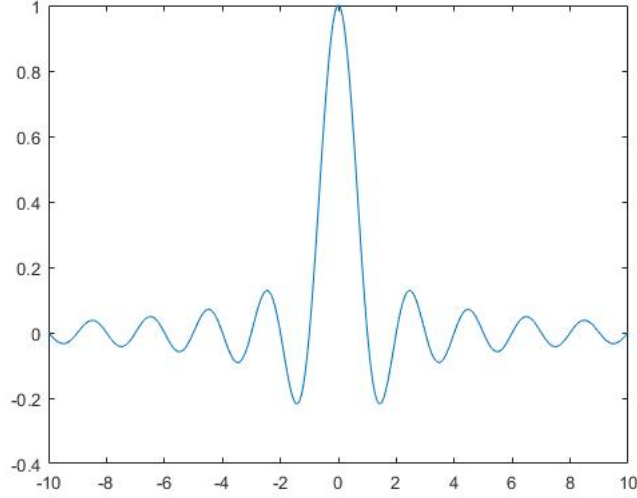


Figure 1.7: $\text{sinc}(x)$

mixing can occur. Similarly, if we include the frequency mismatch in the FWM treatment starting from Eq. 1.21 (adding $e^{i\Delta\omega t}$). The following occurs[4]

$$\hat{\mathcal{H}} = \xi e^{i\Delta\omega t} \hat{b}^\dagger \hat{a}^\dagger + h.c. \rightarrow \frac{\partial \hat{a}}{\partial t} = \xi e^{i\Delta\omega t} \hat{b}^\dagger \rightarrow \frac{\partial^2 \hat{a}}{\partial t^2} = -i\Delta\omega \frac{\partial \hat{a}}{\partial t} + \xi^2 \hat{a}$$

which can be solved to yield

$$\hat{a}(t) = e^{-\frac{1}{2}i\Delta\omega t} \cosh\left(\sqrt{\xi^2 - \frac{1}{4}(\Delta\omega)^2} t\right) \hat{a} + e^{-\frac{1}{2}i\Delta\omega t} \sinh\left(\sqrt{\xi^2 - \frac{1}{4}(\Delta\omega)^2} t\right) \hat{b}^\dagger \quad (1.33)$$

This equation has the form of the squeezing we saw earlier with an adjusted squeezing parameter $s = \sqrt{s_0^2 - \frac{1}{4}(\Delta\omega)^2 \tau}$, where s_0 is the squeezing level with no phase-mismatch[4]. This is another effective bandwidth on the mixing strength, this time in frequency.

1.3.4 Optical Angular Momentum Conservation

If we want to look at the spatial structure of an EM field and the optical orbital angular momentum, we need to solve the Helmholtz equation

$$\nabla^2 \xi + k^2 \xi = 0 \quad (1.34)$$

where ξ is the scalar electric field[9]. Under the paraxial approximation, where we assume the field maintains a small angle with the optical axis, we can make the following substitution[9]

$$\xi(\mathbf{r}) = u(\mathbf{r})e^{ikz} \quad (1.35)$$

where u is the amplitude distribution, and arrive at the following equation

$$\nabla_t^2 u + 2ik \frac{\partial u}{\partial z} = 0 \quad (1.36)$$

where the t subscript indicates the transverse portion of the Laplacian.

In Cartesian coordinates, the natural basis for solutions to this formula are the Hermite-Gaussian (HG) modes.

$$u_{nl}^{HG}(x, y, z) = u_n^{HG}(x, z)u_l^{HG}(y, z) \quad (1.37a)$$

$$u_n^{HG}(x, z) = \frac{C_n^{HG}}{\sqrt{w(z)}} e^{ik \frac{x^2 z}{2(z_R^2 + z^2)}} e^{-\frac{x^2}{w^2(z)}} e^{-i(n+1/2)\chi(z)} H_n\left(\frac{\sqrt{2}x}{w(z)}\right) \quad (1.37b)$$

where $C_n^{HG} = \sqrt{1/(2^n n!)}(2/\pi)^{1/4}$, H_n is the Hermite polynomial of n th order, $w(z)$ is the Gaussian spot size, z_R is the Rayleigh range.

$$w(z)^2 = \frac{2(z_R^2 + z^2)}{kz_R} = w_0^z \left[1 + \left(\frac{z}{z_r} \right)^2 \right]$$

$$z_R = \frac{\pi w_0^2}{\lambda}$$

where λ is the wavelength. This is the most common spatial mode basis for light fields, but HG basis is not an eigenbasis for OAM[9].

An alternate basis, in cylindrical coordinates, that is an eigenbasis for orbital angular momentum[9], is the set of Laguerre-Gauss (LG) modes.

$$u_{mp}^{LG}(\rho, \phi, z) = \frac{C_{mp}^{LG}}{\sqrt{w(z)}} \left(\frac{\rho\sqrt{2}}{w(z)} \right)^{|m|} e^{-\frac{\rho^2}{w^2(z)}} L_p^{|m|} \left(\frac{2\rho^2}{w^2(z)} \right) e^{-ik\frac{\rho^2 z}{2(z_R^2+z^2)}} e^{im\phi} e^{-i(2p+|m|+1)\chi(z)} \quad (1.38)$$

where $C_{mp}^{LG} = \sqrt{2^{|m|+1}p! / [\pi(p+|m|)!]}$ and $L_p^{|m|}$ are the Laguerre polynomials. The phase factor of $e^{im\phi}$ indicates that the LG modes have well-defined orbital angular momentum (OAM), $\langle L_z \rangle = \hbar m$ [9].

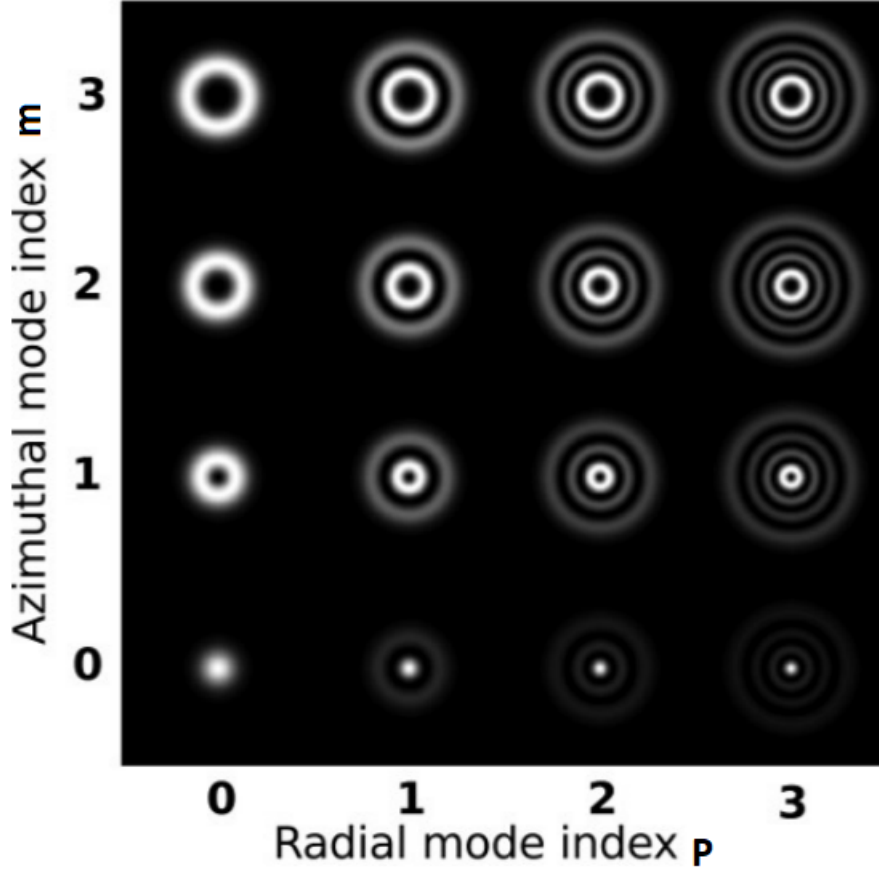


Figure 1.8: LG Modes. [10]

We will be discussing vortices quite a bit later in this paper, which are simply points of zero electric field amplitude surrounded by continuously varying phase[9].

Many optical vortices have the form

$$E \propto r^{|m|} e^{im\phi} e^{-r^2/w^2}$$

where m is the topological charge of the vortex (note the exponential term from the LG modes). A vortex of charge m corresponds to an $LG_{|m|0}$ mode.

$$m = \frac{1}{2\pi} \oint_C \nabla S \cdot d\mathbf{l}$$

and is how many times the phase cycles across the vortex. Also, vortices with charge $|m| > 1$ can be thought of as m single vortices overlapped[9].

Since a charge of m corresponds to a discrete OAM, the FWM process must conserve this quantity[9]. Specifically,

$$2m_0 = m_p + m_c \tag{1.39}$$

where p refers to probe, c to conjugate, 0 to pump.

Chapter 2

Experimental Technique

I will begin by describing the current experimental setup in detail, and then go into the parameters we adjust to get optimal noise suppression. The full schematic is shown in Fig. 2.1.

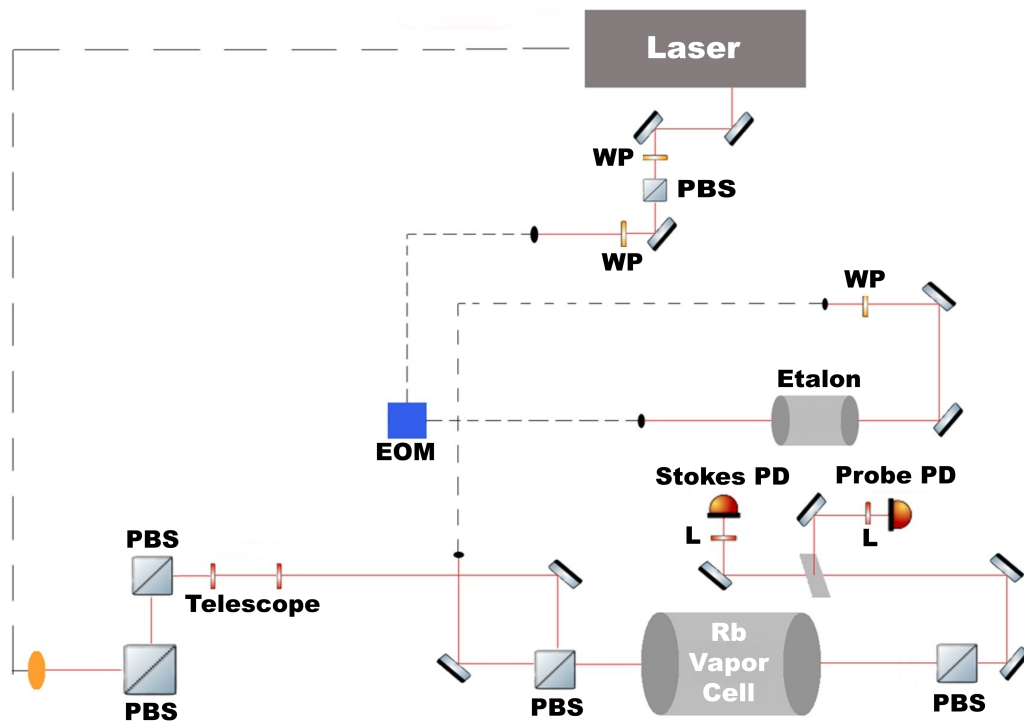


Figure 2.1: Schematic for the experimental setup of this project.

2.1 Setup

We use the same laser to generate the pump and probe input fields, a Toptica TA Pro diode laser. We use two different outputs of the same field; the amplified laser output is used as the pump, and the weak output is used as the probe. We output the pump through a fiber coupler, and use two Polarizing Beam Splitters (PBS) to clean polarization in the field. We then send it through a telescope in order to adjust the beam waist size and position inside the Rb cell.

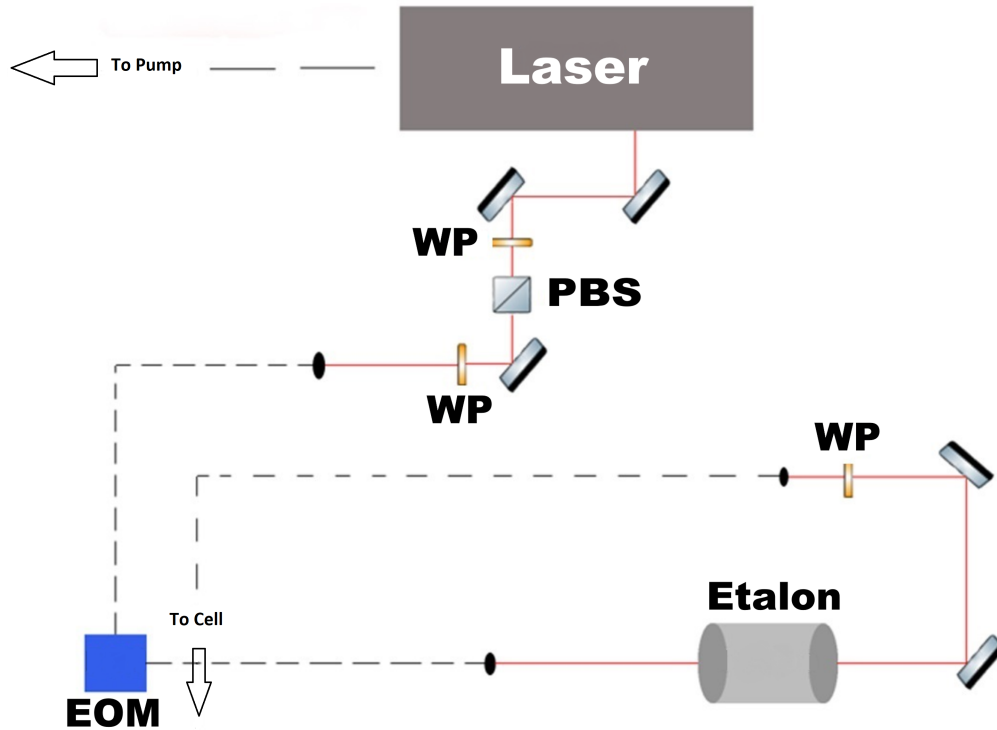


Figure 2.2: Closer look at the probe setup.

For the probe, I will show a closer look at the setup in Fig. 2.2. We use half-waveplates (HWP) to make its polarization perpendicular to the pump, and then couple it to an optical fiber. In the first fiber, we use Electro-optic Modulation (EOM) to shift the frequency of the probe relative to the pump using an RF signal. This is how we control the two-photon detuning referred to throughout. After this

stage, we send the probe through an etalon (a Fabry-Perot interferometer) in order to select the desired frequency (filtering out extra frequencies introduced by the EOM). We then use a final HWP to adjust the polarization before the final fiber.

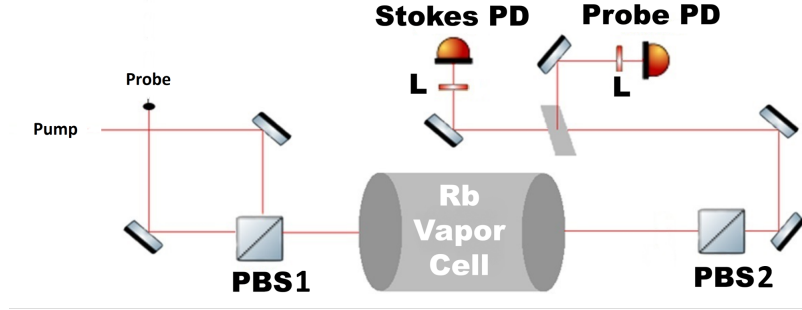


Figure 2.3: Closer look at cell and detection setup.

The cell and detection setup is shown in Fig. 2.3. The probe and pump are then combined on PBS1 at a small angle, and sent through the Rb vapor cell. The cell is surrounded by a three-layer magnetic shield that is thermally stabilized and controlled externally. After the FWM interaction takes place, the three fields exit the cell, and the pump is mostly filtered out using PBS2. From there, since the beams are spatially separated, the probe and Stokes can be sent in different paths using an edge mirror. The probe and Stokes are each focused onto a separate photodetector (PD), with irises used to cut out the remainder of the pump. The PD outputs are then electronically subtracted, and this signal is sent to a spectrum analyzer, where we view the frequency dependent noise.

2.2 Parameter Optimization

The parameters we mainly vary are pump frequency, etalon setting, cell temperature, probe detuning, and probe and pump beam waist positions.

- The pump frequency and etalon setting are linked in that we adjust the etalon

and then tune the pump frequency to get maximal probe transmission. So the etalon is an indirect constraint on the pump frequency we use.

- The cell temperature governs atomic number density in the cell, and therefore the strength of interaction. With high enough density, absorption increases and spontaneous decay effects cause decoherence in the fields.
- The two-photon detuning, controlled via the RF frequency in the EOM, also determines the strength of the interaction and the optical depth of the medium.
- Finally, we adjust the positions of the beam waists of the probe and pump in order to have the best phase-matching conditions, and therefore the highest interaction strength.

2.3 Noise Measurements

We use an HP8596E spectrum analyzer (SA) to analyze our differential signal. The SA takes in a time domain intensity signal and decomposes it into the frequency domain, allowing us to view the power present in our signal at any given frequency in the SA's range. This spectrum represents the noise floor in the optical system. The SA displays its measurements in dBm (power relative to 1 mW in decibels). If we see 4 dBm noise reduction in the system, that corresponds to a 2.5x reduction in the noise floor in base 10. Since the SA shows the power distribution in the system, a differential noise measurement below shot noise for a given intensity is indicative of amplitude squeezing.

Shot noise calibration works as follows:

- Send a beam with a well-known power to a 50-50 beam splitter.
- Propagate each arm to a separate photodiode.

- Electronically subtract the two signals.
- Average the spectrum on the SA on the frequency range of interest (in our case 100 kHz-500 kHz).
- Repeat for different input powers.

This is an effective measurement of shot noise because once the two fields of equal magnitude are subtracted, the classical noise of the system is eliminated, leaving just the quantum noise of the system. Imbalances in the detection will skew the measurements high, as this introduces classical noise into the differential signal. We use the frequency range of 100 kHz-500 kHz because it avoids most of the noise present in our environment (low frequency, other electronic noise from nearby).

2.4 OAM Experiment

In order to examine the orbital angular momentum conservation of the system, we need to input fields with OAM. We can either input OAM-bearing probe, pump, or both. For the pump field, we use a phase mask to impart a charge of $m = \pm 1$. This mask has a gradually changing index of refraction that changes the phase of the field azimuthally. The chirality of the vortex can be controlled by which direction the mask faces relative to the optical axis. For the probe, for the first set of measurements, we used the phase mask and imparted a charge of $m = +1$. For the later sets where we also had a vortex on the pump, we used a diffraction grating to generate different orders of vortices and choose the first order which corresponds to $m = -1$. See Fig. 2.4 for reference.

In order to see the fields that are output from the Rb cell, we placed a camera into the residual transmission of a mirror after PBS2 to view the output beams. For most of our measurements, we use the interference method described in Vasnetsov[11]

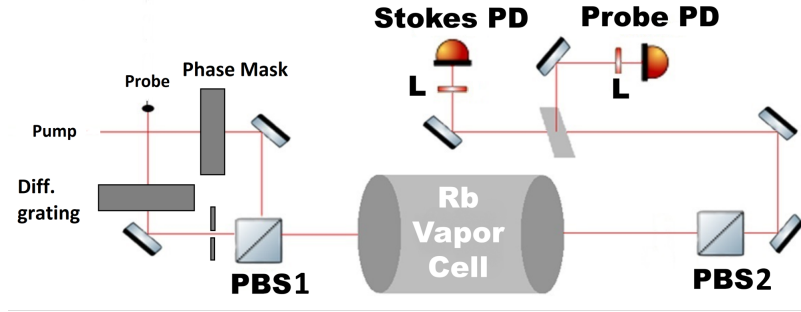


Figure 2.4: Schematic with the diffraction grating in the probe path and the phase mask in the pump path.

to more easily measure the angular momentum present in each field. For the probe, we split the field before PBS1 and send this around the cell. We then use a mirror to overlap this new field with the probe output from the cell. For the Stokes, we introduce a flip mirror after the mirror after the cell, expand the field with a lens, and then choose a small portion of the beam away from the vortex to interfere with the leak Stokes from before.

For the tilted lens method[12], we expect images similar to Fig. 2.5. For a charge of 1, we expect the beam to split into two lobes, with the line separating them on a diagonal. For charge 2, we expect three lobes with two separating lines. For charge 3, we expect 4 lobes with three separating lines. For the opposite chirality, we expect to see the mirror image. Since it can be hard to tell a vortex from some other beam defect, and since the tilted lens method can be difficult to precisely and repeatedly use, we use the interference method, for most of our measurements.

For the interference method, we expect forks in the interference fringes to form at any vortices, as in Fig. 2.6. For vortices of charge 2, we expect to see a double fork (three fringes converging to one), and for charge 3 we expect a triple fork (four fringes converging to one).

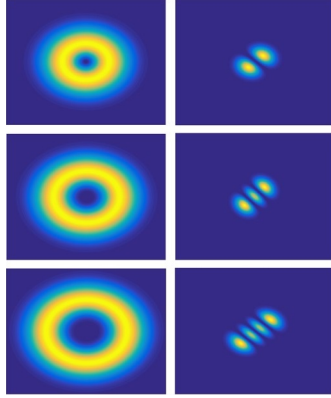


Figure 2.5: Top row: charge 1, with and without tilt; middle row: charge 2, with and without tilt; bottom row: charge 3, with and without tilt. [13]

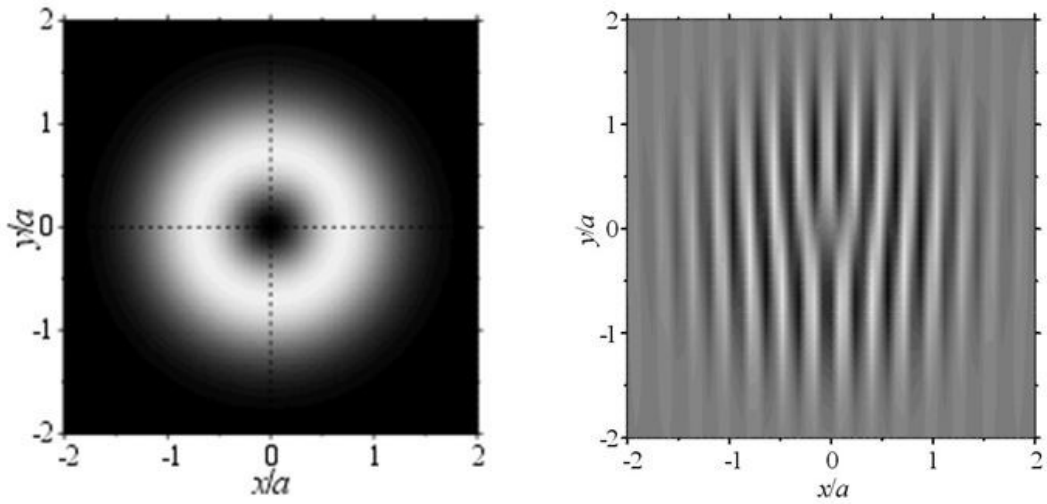


Figure 2.6: Left: LG_{01} mode without interference; right: the same mode interfered with a plane-wave. [14]

Chapter 3

Intensity Squeezing Optimization

3.1 Preliminary Results

We originally observed squeezing in Spring '17, but our initial squeezing measurements were done with an improperly calibrated shot noise. The two parameters that we mainly varied initially were cell temperature and pump frequency/etalon tuning. We looked at temperatures of 92 °C, 96 °C, 100 °C, 110 °C. At the time we thought we saw higher noise at 110 °C than at the other temperatures; this is also near the safe temperature limit for our cell.

Fig. 3.1 shows the data set that had the among the best squeezing when calculated with the shot noise calibration we had at the time. The black line shows the differential noise between the probe and Stokes fields. The red line shows the differential noise between two independent fields, the SNL for a particular intensity of the probe and Stokes. Since the black line is below the quantum noise limit, we say that we have intensity squeezing, and we know that the probe and Stokes are quantum correlated. In low frequencies, we saw what appeared to be -4.5 dB of squeezing.

We realized, though, that the shot noise should have a flat noise spectrum in the examined frequency region, and we were concerned with the slope in the shot noise in Fig. 3.1. Recalibrating our data, we saw that we had overestimated shot noise, and

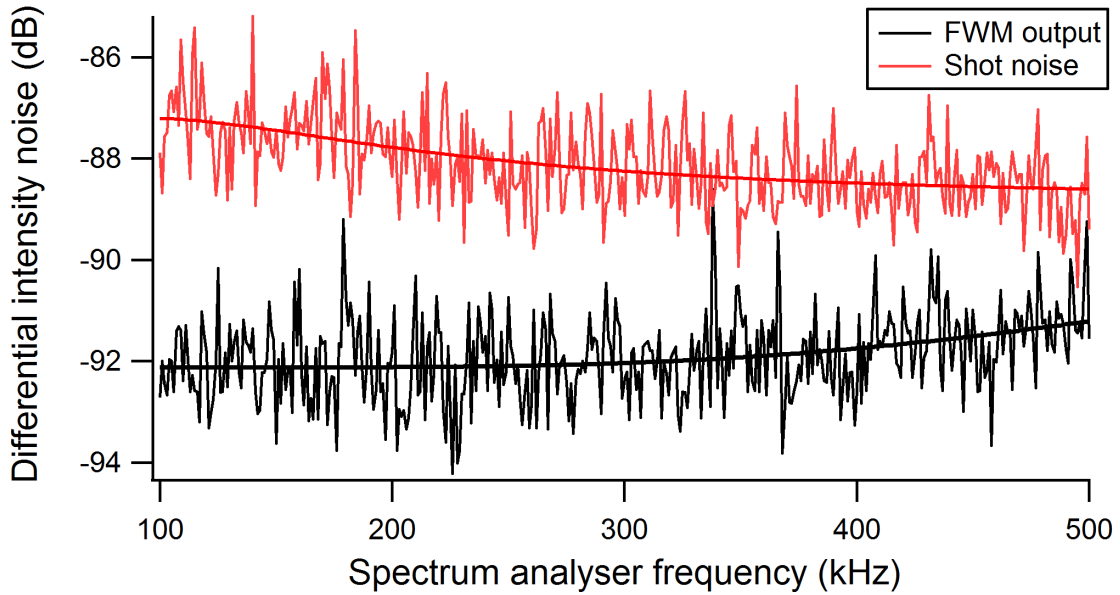


Figure 3.1: Differential noise between Stokes and probe in black, and the quantum shot noise limit in red. We see as much as -4.5 dB of squeezing.

had therefore overestimated squeezing.

3.2 Shot Noise Recalibration and Results

Our initial shot noise calibration and our subsequent recalibration and fit are shown in Fig. 3.2

We can see in the graph that our initial shot noise calibration overestimated the SNL for lower powers. Armed with this new calibration, I went back and reanalyzed the data from 2017. This is shown in Fig. 3.3-Fig. 3.5. These figures feature both squeezing vs two-photon detuning (left axis) and probe and Stokes signal strength vs two-photon detuning (right axis). As I talked about in Ch. 1.3.3, the two-photon detuning determines the strength of the FWM interaction. The relationship between this detuning and squeezing is not quite that simple, however. While Eq. 1.30 gives the degree of squeezing considering only the effects of the FWM process we are interested in, and this depends only on the gain on the probe, other gain processes can contribute

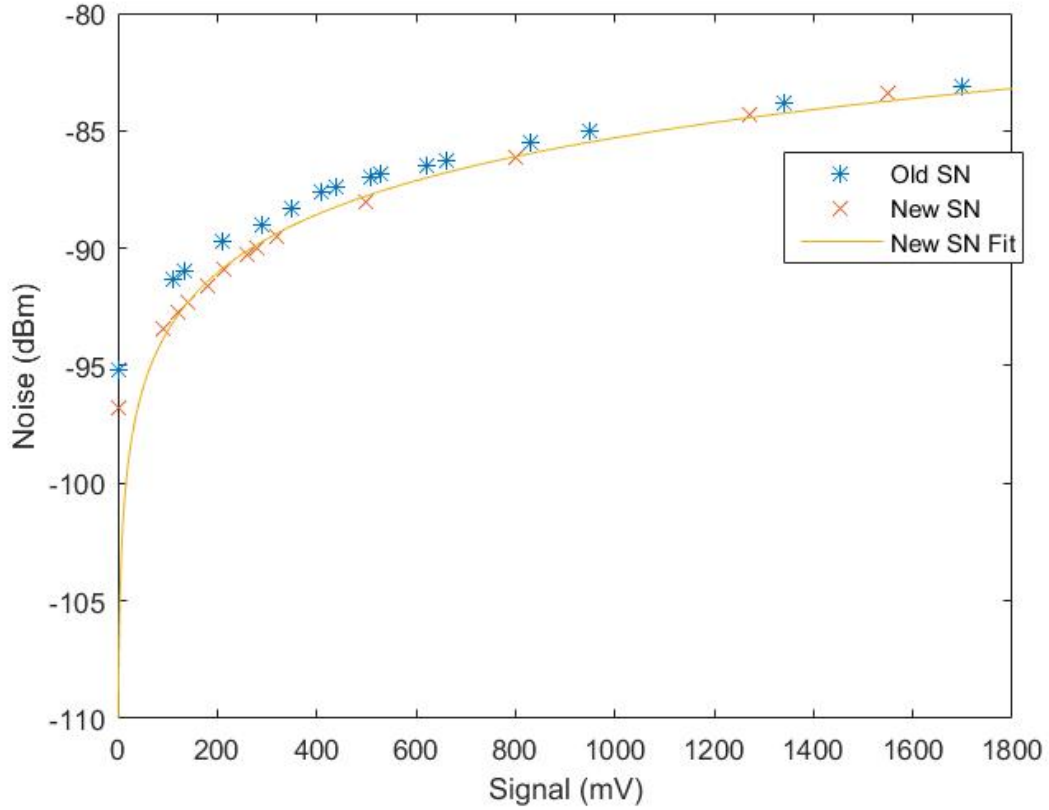


Figure 3.2: Shot noise calibrations.

uncorrelated noise to the fields. Because of this, the area of highest gain will not be the area of best squeezing. As we tune further away from highest gain, however, we expect worse squeezing, as the interaction strength begins to wane. We expect a parabolic trend for squeezing vs two-photon detuning. We also expect our best squeezing to happen with well-balanced probe and Stokes intensities, though we don't see this in every case.

It turns out that we the highly overestimated squeezing was at 92 °C and 96 °C. While we don't see the same maximum squeezing for 100 °C that we thought we had, we do see squeezing of up to -2.8 dB. I also reanalyzed the data at 110 °C, which can be found in Fig. 3.6. The x-axis for this plot is the detuning from the hyperfine

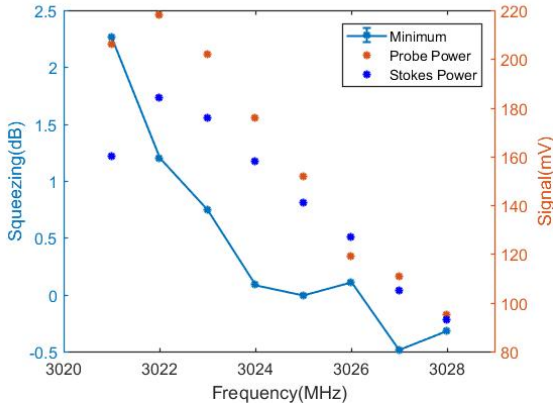


Figure 3.3: Squeezing vs detuning with cell temperature of 92 °C. The left axis corresponds to the squeezing level of each measurement, and the right axis corresponds to the signal strength of probe and Stokes of each measurement. The x-axis corresponds to the two-photon detuning, or how far the probe is detuned from the pump frequency.

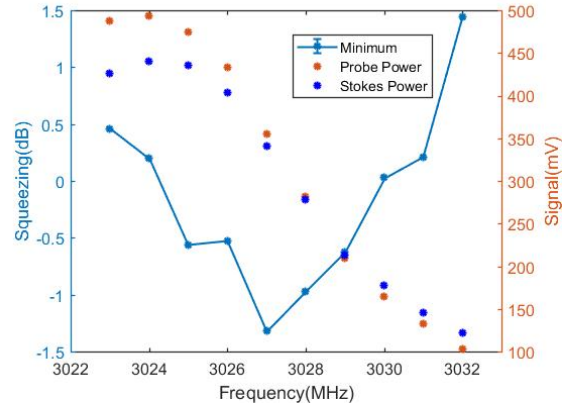


Figure 3.4: Squeezing vs detuning with cell temperature of 96 °C. The left axis corresponds to the squeezing level of each measurement, and the right axis corresponds to the signal strength of probe and Stokes of each measurement. The x-axis corresponds to the two-photon detuning, or how far the probe is detuned from the pump frequency.

resonance (0 MHz corresponds to 3035 MHz in the other plots). It turns out that the noise in this region wasn't as high as we once thought, though we still don't want to push the physical limits of the system. From this information, we decided to start working at 100 °C.

From here we took great pains to adjust the beam waists of the pump in probe in order to have the best phase matching conditions possible. The optimal configuration ended up being the following: the pump waist slightly larger than the probe waist, the pump waist position slightly outside the shielding of the cell, and the probe waist in the cell. This was achieved by adjusting the telescope for the pump and adjusting the output coupler focus for the probe. The best results we got for this section of the experiment is shown in Fig. 3.7. The error bars for this data represent one standard deviation in the squeezing value across 5 measurements. The best squeezing we have had to date was -4.1 dB, which can be seen in Fig. 3.8. These measurements were taken with pump power of 350 mW and cell temperature of 100 °C.

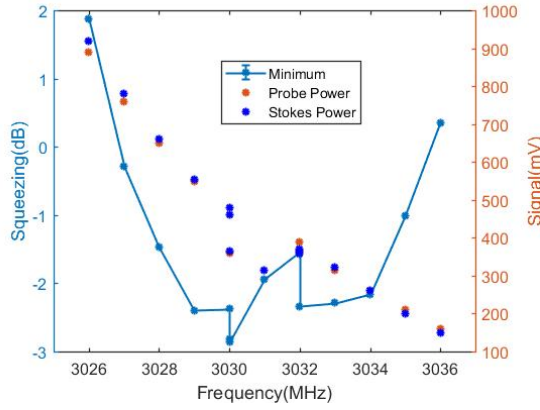


Figure 3.5: Same as Fig. 3.3, except the cell temperature was 100 °C. The x-axis corresponds to the two-photon detuning, or how far the probe is detuned from the pump frequency.

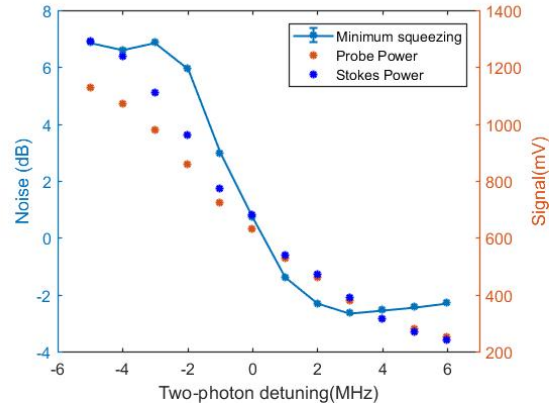


Figure 3.6: Same as Fig. 3.3, except the cell temperature was 110 °C. The x-axis is defined as the two-photon detuning as defined in Fig. 3.3 minus the hyperfine splitting frequency of 3035 MHz.

3.3 Power Dependence of Squeezing

We also looked at the dependence of squeezing on the input pump power. This is an important parameter for the future of the experiment, as we will need to operate under tighter power constraints. We changed the power input while attempting to hold other parameters constant, and took squeezing measurements across two-photon detunings. These are shown in Fig. 3.9-Fig. 3.12. We went from 450 mW to 175 mW. We can see that there is a slight drop in squeezing level as we decrease power, from -2.5 dB to -1.8 dB. It is worth noting that these measurements were taken before we reanalyzed our old data and decided to move to 100 °C, and so was taken at 96 °C. Also note that we started with -2.5 dB squeezing at 450 mW, and so were not in a region with the best squeezing to start with.

From these results, it seems plausible to maintain a significant degree of squeezing with lower pump power. With more precise adjustments at each power, we should also be able to increase the level of squeezing.

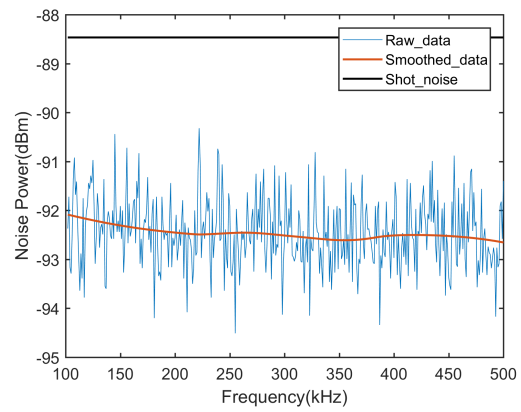
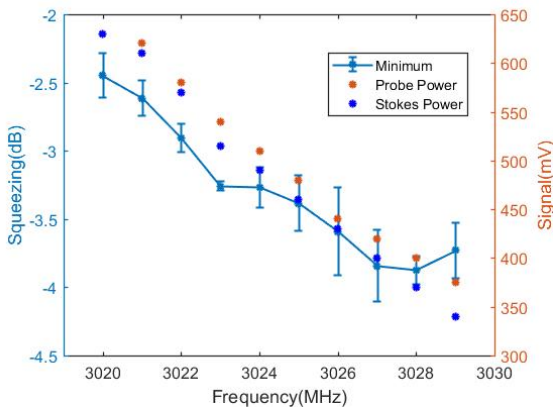


Figure 3.7: Best squeezing vs detuning results (pump power of 350 mW, $T = 100\text{ }^{\circ}\text{C}$). The axes are defined the same as in Fig. 3.3. Figure 3.8: Best squeezing so far. The blue line is the raw data, black line is SNL for input power, red line is smoothed differential noise data.

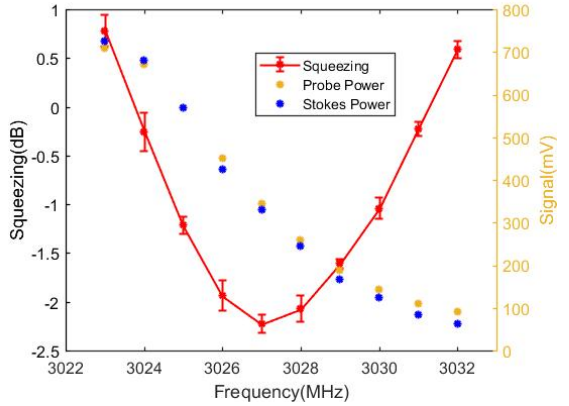
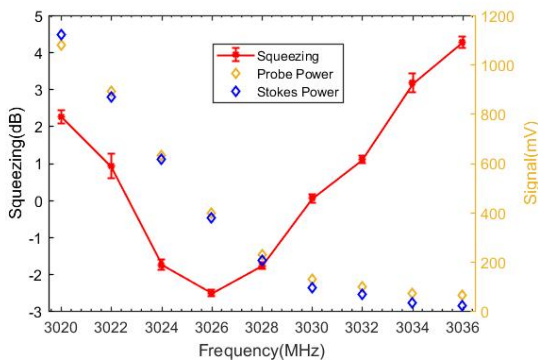


Figure 3.9: Squeezing vs detuning with 450 mW pump power. The axes are defined the same as in Fig. 3.3. The cell temperature was $96\text{ }^{\circ}\text{C}$.

Figure 3.10: Same as Fig. 3.9, except the pump power was 390 mW.

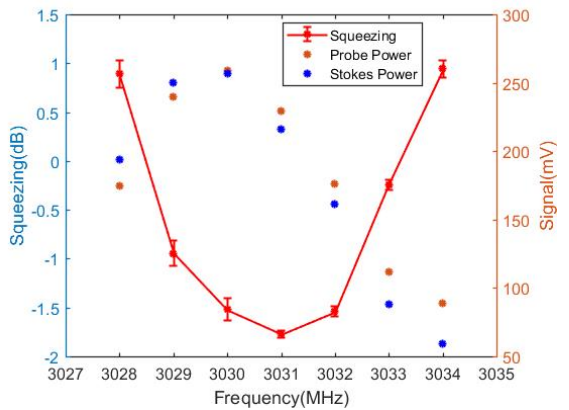
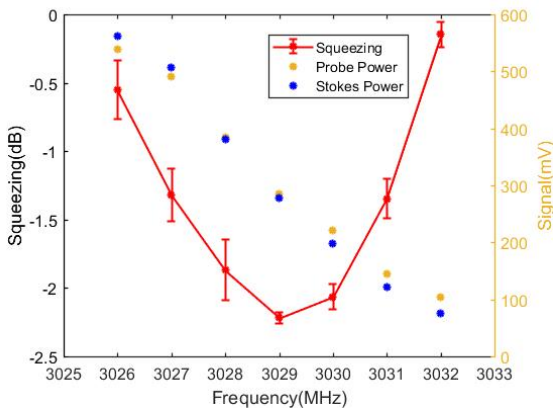


Figure 3.11: Same as Fig. 3.9, except the pump power was 295 mW.

Figure 3.12: Same as Fig. 3.9, except the pump power was 175 mW.

Chapter 4

OAM Results

Recall the setup in Ch. 2.4. For this part of the experiment, we input pump and probe beams to the FWM setup with different OAM. m_p refers to the OAM of the probe, and m_0 refers to the OAM of the pump. We took data for 4 configurations: $m_p = +1, m_0 = 0$; $m_p = 0, m_0 = -1$; $m_p = -1, m_0 = -1$; $m_p = -1, m_0 = +1$. For each of these, I will show plots of the intensity profiles of the probe and Stokes for multiple detunings, as well as the squeezing vs detuning. Note that the introduction of vortices changes the beam sizes for the effected beam, and requires adjustments in the beam waist size and locations order to maintain good phase-matching conditions. For these data sets, the x-axes will be in terms of detuning from the hyperfine resonance of 3035 MHz.

4.1 Input Probe Beam Carrying a Vortex

We took this data before we started using the interference method, so I will show images from the lens tilt method. Since we input $m_p = +1, m_0 = 0$, we expect to get $m_c = -1$ to conserve OAM. For a tilted lens setup, we expect two lobes to develop on a diagonal in a field with a vortex of charge 1. For the opposite chirality, we expect the opposite tilt.

The tilted lens data for three different detunings is shown in Fig. 4.1-Fig. 4.3. We

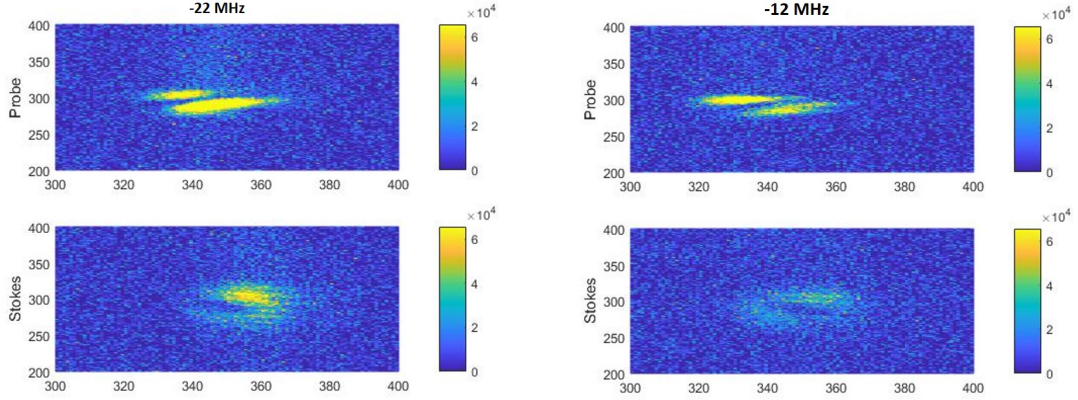


Figure 4.1: Beam profiles of probe and Stokes at -22 MHz for vortex in probe input. Figure 4.2: Beam profiles of probe and Stokes at -12 MHz for vortex in probe input.

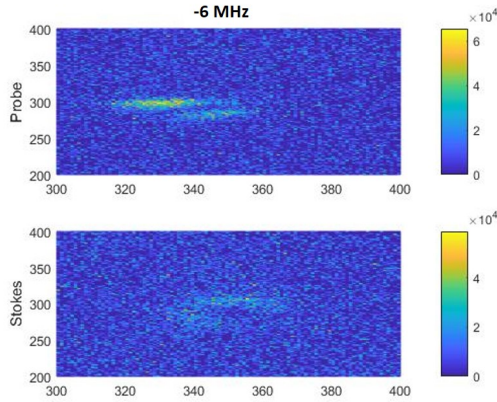


Figure 4.3: Beam profiles of probe and Stokes at -6 MHz for vortex in probe input.

note that as we move the two-photon detuning closer to the resonance, the intensity in the probe moves from the bottom-right lobe to the top-left lobe; the Stokes intensity moves from the top-right to the bottom-left. It is also apparent, especially in Fig. 4.2, that the probe and Stokes have the opposite tilt, and therefore the opposite chirality. This matches up with the theoretical conservation of OAM (Eq. 1.39, $m_0 = 0$, $m_p = +1$, $m_c = -1$).

The squeezing for this is shown in Fig. 4.4. The highest squeezing we see for this data set is -3.5 dB. This configuration yielded the highest overall squeezing of the 4, with -3.8 dB.

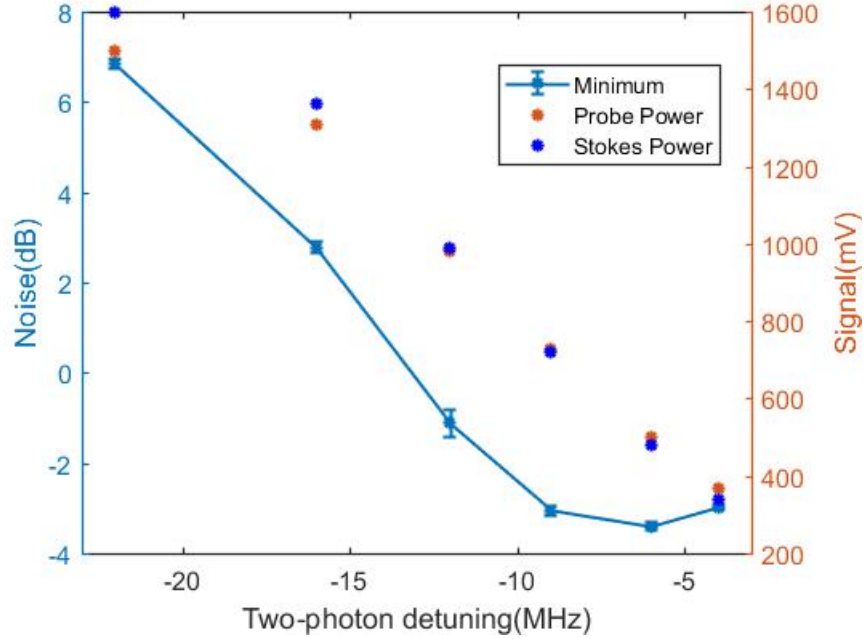


Figure 4.4: Squeezing vs detuning with vortex of $m = +1$ on the probe input. The left axis corresponds to the squeezing level for each measurements, and the right axis corresponds to the signal strength of the probe and Stokes for each measurement. The x-axis is the two-photon detuning minus the hyperfine splitting frequency of 3035 MHz.

4.2 Pump Beam Carrying a Vortex

We did use the interference method to measure the OAM for this data set. Graphs for different detunings are shown in Fig. 4.5-Fig. 4.8, with the Stokes on the left, pump in the center, and probe on the right. For this configuration, since we input pump with $m_0 = -1$, and $m_p = 0$, we expect a Stokes with $m_c = -2$ to conserve OAM (Eq. 1.39). This means we expect to see no forks in the probe interference pattern, and either two single forks or one double fork in the Stokes interference pattern.

For most of the detunings, we see what we expect: 0 charge in the probe and charge of 2 in the Stokes. This satisfies Eq. 1.39, $m_0 = -1$, $m_p = 0$, $m_p = -2$. These are visible in the forks in the interference pattern on the Stokes. As we tune closer to the resonance, the vortices in the Stokes move closer together, almost overlapping.

For -85 MHz, we see some odd features. Instead of $m_p = 0, m_c = -2$, we see $|m_p| = 5, |m_c| = 3$. We believe this is due to improper alignment and beam size matching. For OAM-bearing beams, we believe that matching the beam sizes of the pump and probe in the cell is important for the conservation of OAM in the dominant modes of the fields.

The squeezing for this data set is shown in Fig. 4.9.

We see that these points are above shot noise. It should be noted that there was significant leak of the pump into the Stokes channel for these measurements. The beam sizes of different charges were also mismatched. The best squeezing for this configuration was -1.2 dB, not shown here.

4.3 Probe and Pump with Same Charge Vortex

For this configuration ($m_p = -1, m_0 = -1$), we expect a Stokes field output with $m_c = -1$, in order to satisfy Eq. 1.39. This means we expect to see one fork in the interference fringes of both the probe and the Stokes. Graphs with the probe and Stokes with and without interference for different detunings are shown in Fig. 4.11, Fig. 4.12, Fig. 4.13. The squeezing measurements for this data set are shown in Fig. 4.10.

We can see that the best squeezing level is about -2.4 dB. We see conservation of OAM for all of these detunings, satisfying Eq. 1.39 with $m_0 = -1, m_p = -1, m_c = -1$. We see single forks in the interference patterns of the probe and Stokes, indicating the charges of the fields. We also see that the fields become more evenly amplified across their profiles as we tune toward better squeezing.

4.4 Probe and Pump with Opposite Charge Vortex

For this configuration ($m_p = -1, m_0 = +1$), we expect a Stokes field output with $m_c = +3$, by Eq. 1.39. This means we expect a single fork in the probe interference pattern, and either a triple fork, one double fork and two single forks, or three single forks in the Stokes interference pattern. Graphs with the probe and Stokes with and without interference for different detunings are shown in Fig. 4.15, Fig. 4.16, Fig. 4.17. The squeezing measurements for this data set are shown in Fig. 4.14.

The best squeezing for this set is about -2 dB. In each of these graphs, we can see that OAM is conserved (Eq. 1.39, $m_0 = +1, m_p = -1, m_c = +3$). As we tune through the probe frequencies, it seems that the Stokes charges move together and overlap at -7 MHz. Here we see a single fork and a double fork, which corresponds to a single vortex and a double vortex, which suggests that the Stokes is partially composed of the LG_{02} mode at this frequency. This seems to agree with the theory I mentioned at the end of Ch. 1.3.4. We also observe that the images clean up (more even amplification across the profiles) as we move toward the area of better squeezing.

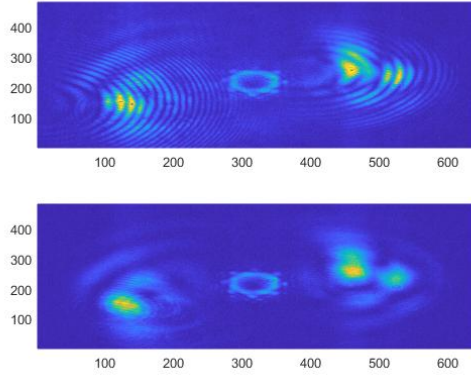


Figure 4.5: Beam profiles of Stokes, pump, and probe at -85 MHz for vortex in pump input. Stokes on left, pump in center, probe on right. Interfered with plane-waves on top, without interference on bottom.

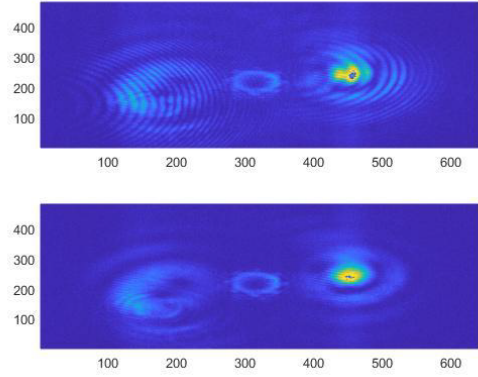


Figure 4.6: Beam profiles of Stokes, pump, and probe at -55 MHz for vortex in pump input. Stokes on left, pump in center, probe on right. Interfered with plane-waves on top, without interference on bottom.

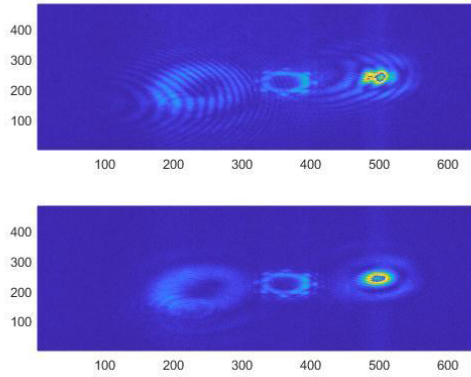


Figure 4.7: Beam profiles of Stokes, pump, and probe at -25 MHz for vortex in pump input. Stokes on left, pump in center, probe on right. Interfered with plane-waves on top, without interference on bottom.

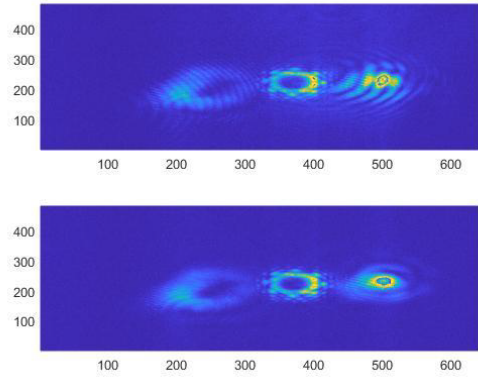


Figure 4.8: Beam profiles of Stokes, pump, and probe at -5 MHz for vortex in pump input. Stokes on left, pump in center, probe on right. Interfered with plane-waves on top, without interference on bottom.

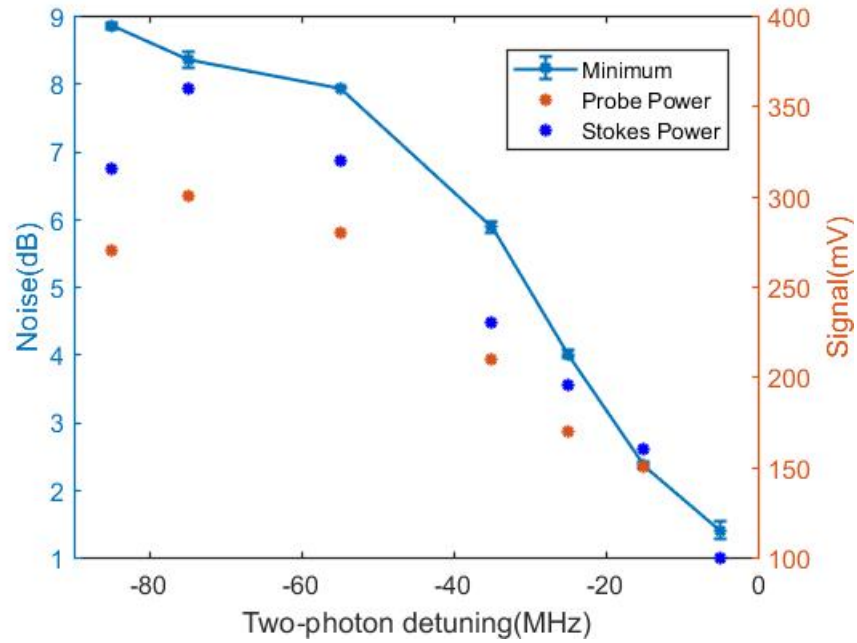


Figure 4.9: Same as Fig. 4.4, but with vortex of $m = -1$ on the pump input and no vortex on the probe input.

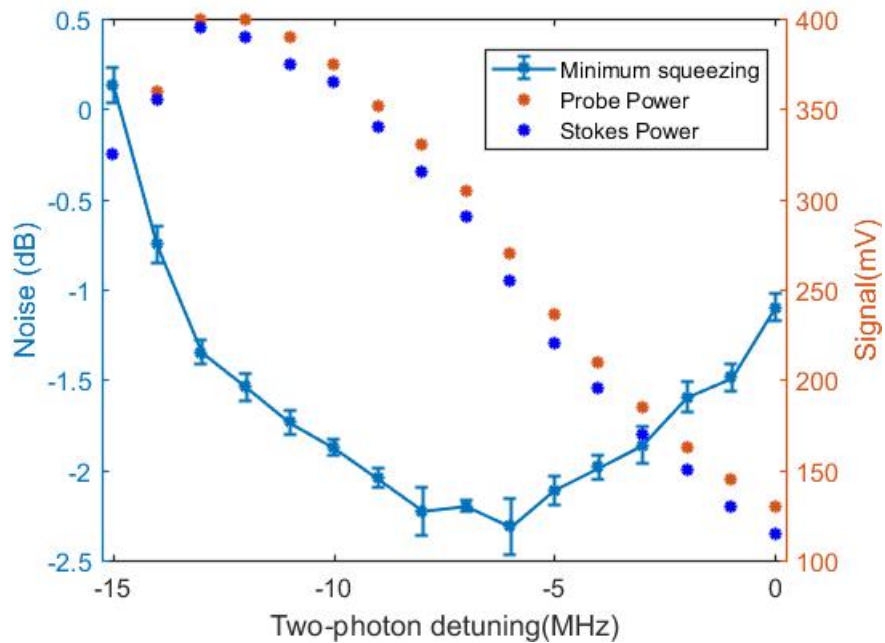


Figure 4.10: Same as Fig. 4.4, but with vortex of $m = -1$ on both input fields.

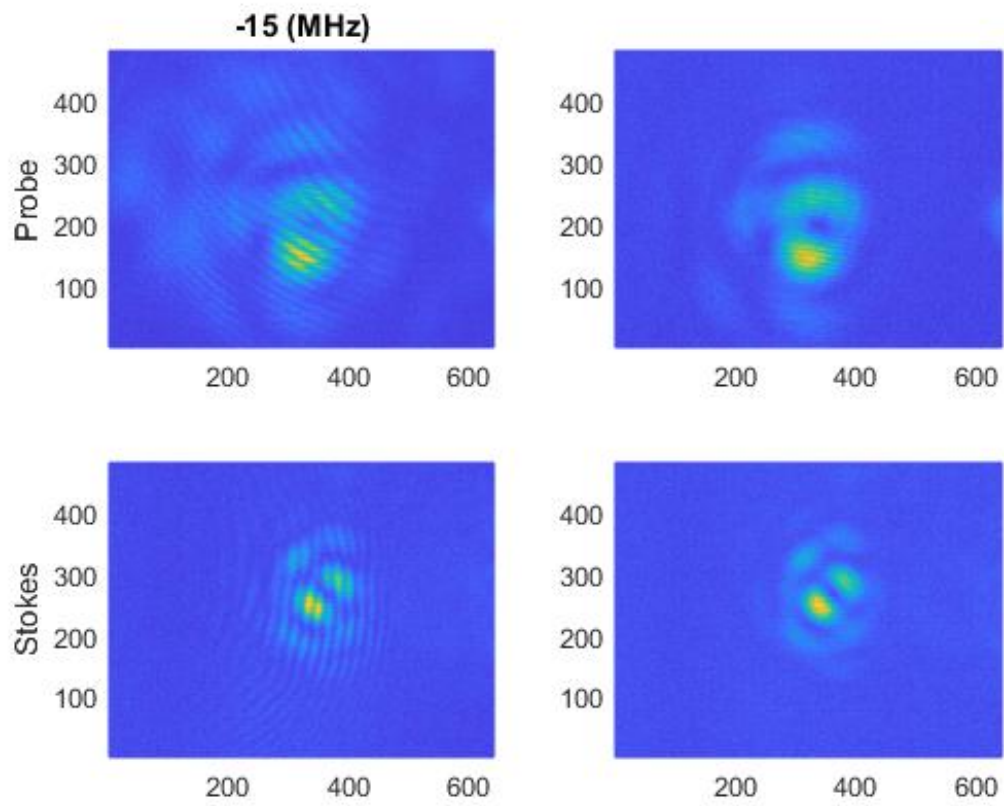


Figure 4.11: Beam profiles of probe and Stokes with (left) and without (right) interference at -15 MHz for same charge in pump and probe input.

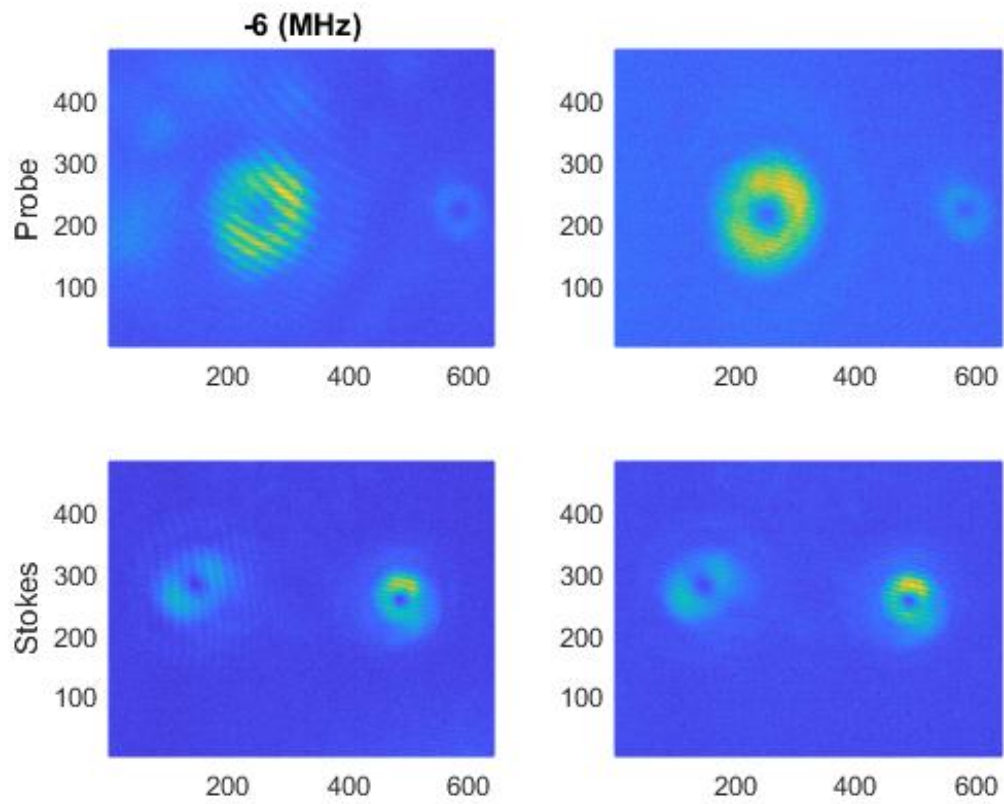


Figure 4.12: Beam profiles of probe and Stokes with (left) and without (right) interference at -6 MHz for same charge in pump and probe input. The Stokes is the beam on the left in its images.

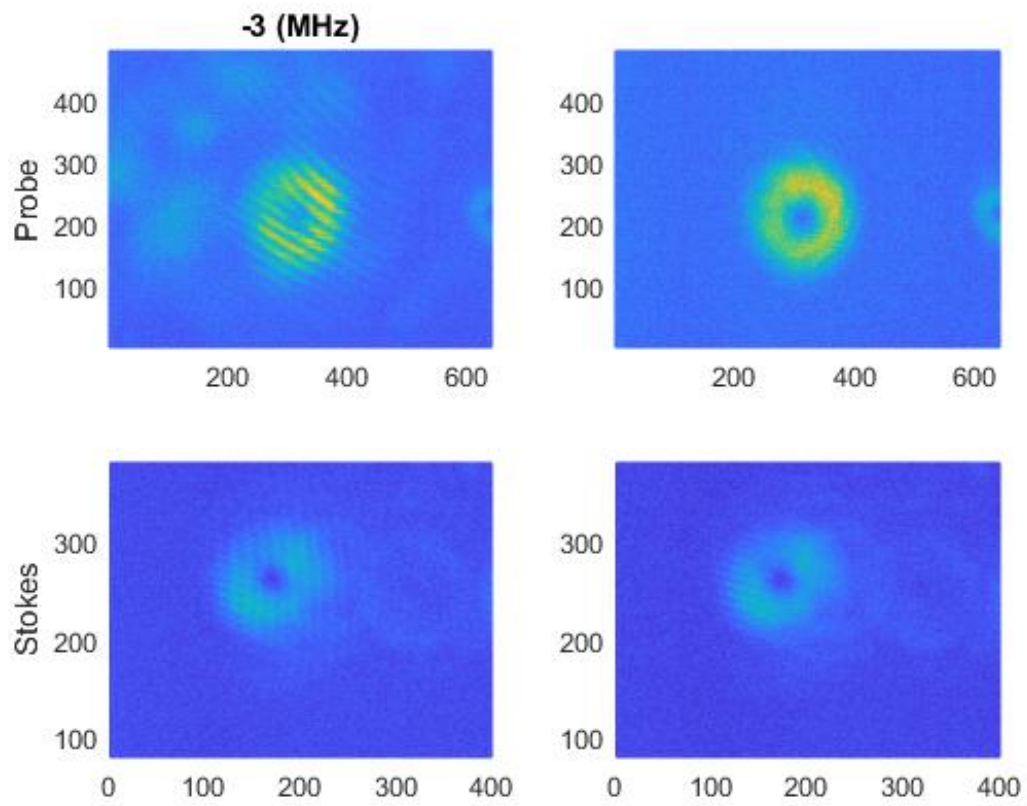


Figure 4.13: Beam profiles of probe and Stokes with (left) and without (right) interference at -3 MHz for same charge in pump and probe input.

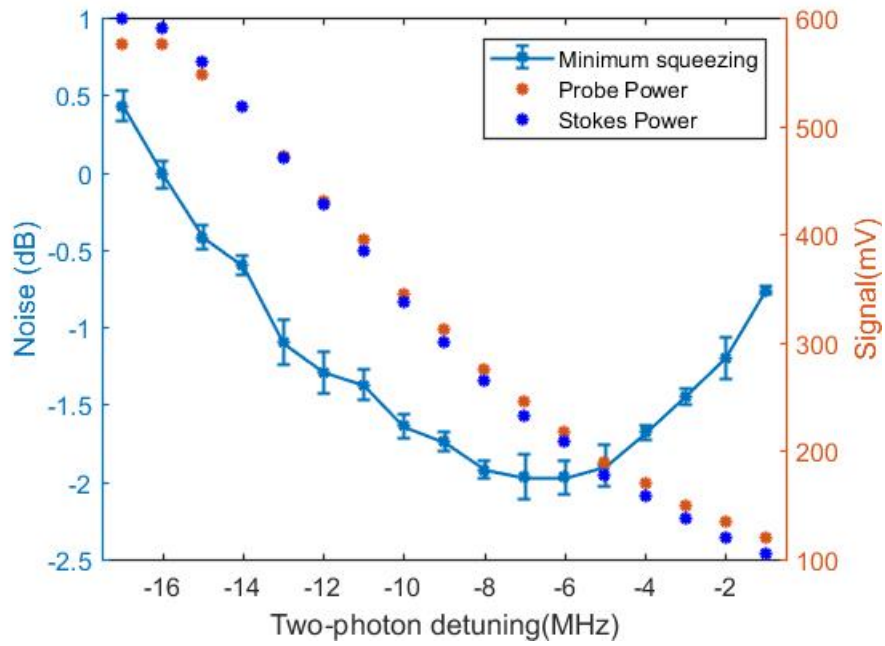


Figure 4.14: Same as Fig. 4.4, but with vortex of $m = -1$ on probe input field, $m = +1$ on pump input field.

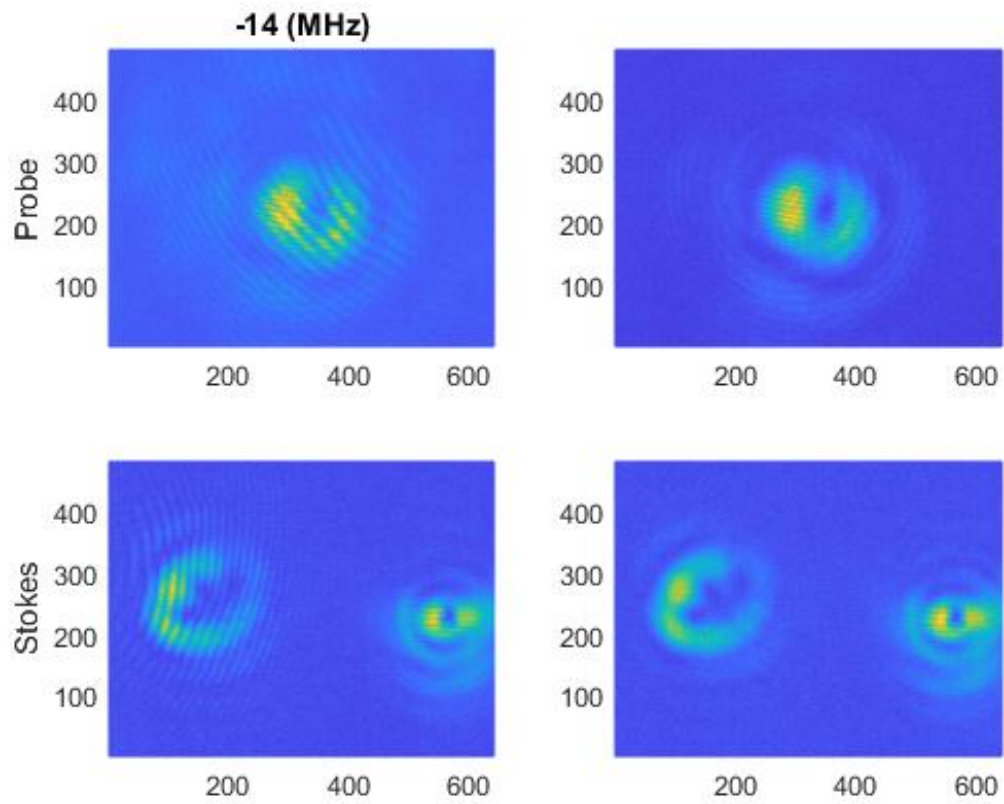


Figure 4.15: Beam profiles of probe and Stokes with (left) and without (right) interference at -14 MHz for opposite in pump and probe input. The Stokes field is on the left of its images.

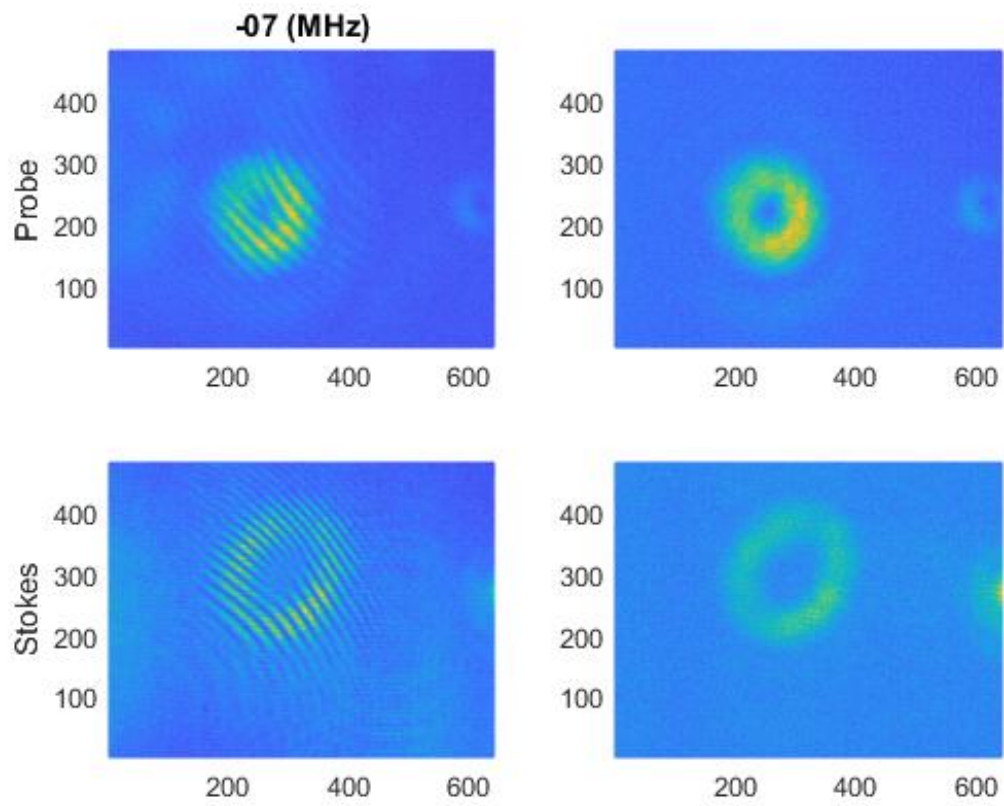


Figure 4.16: Beam profiles of probe and Stokes with (left) and without (right) interference at -7 MHz for opposite charge in pump and probe input.

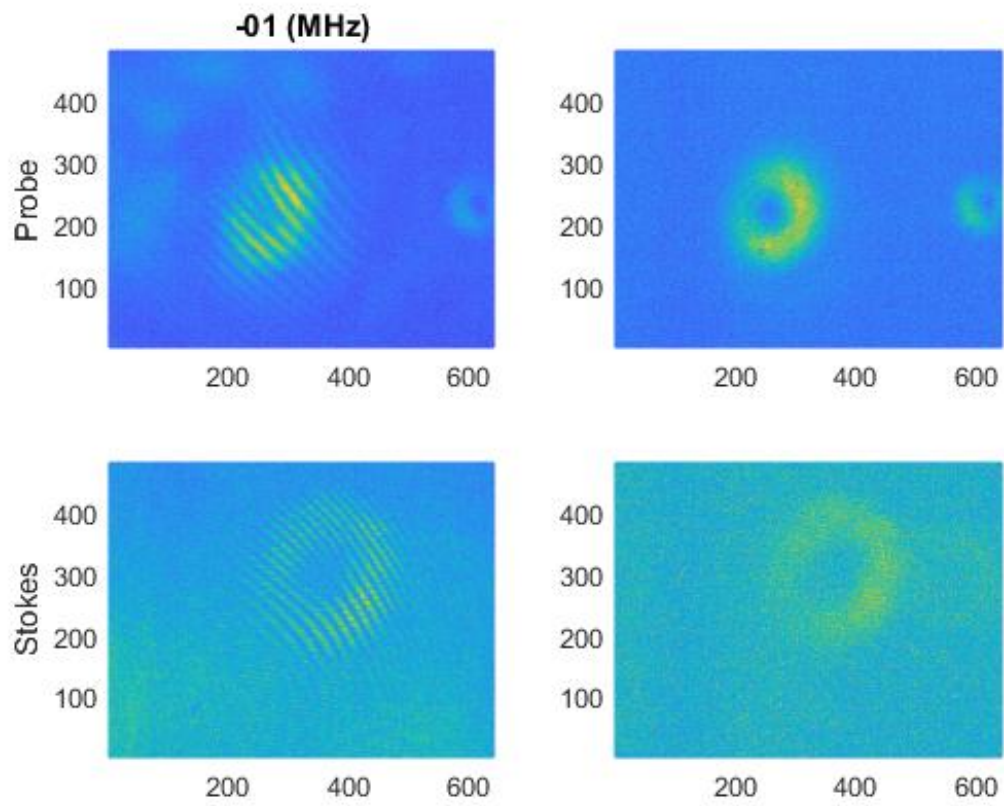


Figure 4.17: Beam profiles of probe and Stokes with (left) and without (right) interference at -1 MHz for opposite charge in pump and probe input.

Chapter 5

Conclusions

Although our degree of squeezing is not as high as we had first thought, -4.1 dB is a significant achievement. We have found that the positions and sizes of the beam waists for the input fields matters a great deal for the level of squeezing. Our data indicates that a cell temperature of 100 °C yields the best squeezing. We also examined the dependence of squeezing on the power of the input pump field. While we see a slight degradation of squeezing quality with decreased intensity, we were still able to maintain -1.8 dB (vs -2.5 at the highest power for this set of measurements) at low power. From these results, it seems reasonable to say that we have observed intensity squeezed light in a wide range of experimental conditions.

For the OAM portion of our experiment, we have looked at four different configurations: vortex in probe alone, vortex in pump alone, vortices in both with equal chirality, vortices in both with opposite chirality. Our best squeezing results among those configurations was with the vortex in the probe alone. We saw up to -3.8 dB of squeezing. We saw the OAM we expected to, with a vortex in the Stokes of the opposite chirality of that of the probe. In this case, as we changed detuning the intensity of the probe and Stokes shifted from one side of their profiles to the other. For the vortex in the pump alone, we saw our worst squeezing at -1.2 dB, but we had significant pump leak in our Stokes detector. At the furthest detuning from the

hyperfine resonance we saw a strange structure develop with 3 vortices in the Stokes and 5 in the probe, which is not what we expect. This is probably due to improper alignment and beam waist matching. For the other frequencies, we saw what we expected, with 2 vortices developing in the Stokes. As we moved towards the area of highest squeezing, these vortices started to converge. Our best squeezing for vortices in both channels with the same chirality was -2.4 dB. For this case, we see the OAM generated in the Stokes that we expect. We saw more evenly amplified probe and Stokes across their profiles as we tuned towards higher squeezing. The best squeezing for opposite chirality was -2 dB. We saw the OAM we expected in the Stokes, with 3 vortices developing. We also saw these move closer together as we approached the region of highest squeezing. Two of them converged into a double vortex.

5.1 Future Plans

In the immediate future, we will use a spatial light modulator (SLM) to explore the effects of different input OAMs. These can be used to create a more general spatial phase pattern and allow us to input probes with various OAM structures.

The long term goals of this experiment are to generate the polarization Bell states.

5.1.1 Bell States

The Bell states are a basis for two-field entanglement, shown in Eq. 5.1 and Eq. 5.2, and correspond to 0 and 1 in a single bit basis. In the equations, $|H\rangle$ refers to the horizontally polarized state and $|V\rangle$ refers to the vertically polarized state, and the subscripts P and S refer to probe and Stokes respectively. The first equation is the superposition of parallel probe and Stokes, and the second equation is the superposition of perpendicular probe and Stokes. They are essential to realize quantum information, as information can be encoded in the superposition of the Bell states.

$$\frac{1}{\sqrt{2}}(|H\rangle_P |H\rangle_S \pm |V\rangle_P |V\rangle_S) \quad (5.1)$$

$$\frac{1}{\sqrt{2}}(|H\rangle_P |V\rangle_S \pm |V\rangle_P |H\rangle_S) \quad (5.2)$$

5.1.2 Polarization Entanglement

This will require us to double our setup in order to incorporate the Faraday polarization controller device made in previous work on this project, and to recombine the different modes. The general design we will look to implement is a dual-rail system. This requires us to split the probe in two and the pump in two, to perpendicularly polarize one probe with respect to the other, and one pump with respect to the other, and to send all four of these fields through our cell without overlap. We must then create a scheme that allows us to achieve each of the Bell states. Since multiple Bell states cannot be realized at the same time, we want to make it easy to switch between them. This will require various phase and polarization shifts, using wave-plates and polarizers, as well as a physical recombination of the four fields. In order to realize this setup, each arm needs to be given adequate power for the FWM process to occur efficiently. This means we will need to work at half of our maximum power in each arm.

Bibliography

- [1] R. Loudon. The quantum theory of light. Oxford; New York: Oxford University Press; 2000.
- [2] M. Turnbull. *Multi-Spatial-Mode Quadrature Squeezing from Four-Wave Mixing in a Hot Atomic Vapour* (School of Physics and Astronomy, University of Birmingham, Birmingham UK, 2013)
- [3] V. Fock. Note to the Quantification of the harmonic Oscillator in a Magnetic Field. *Zeitschrift Fur Physik*. 1928 May;47(5-6):446-448.
WOS:000207399000013.
- [4] M. Jasperse. *Relative Intensity Squeezing by Four-Wave Mixing in Rubidium* (School of Physics, The University of Melbourne, Melbourne AU, 2010)
- [5] R.W. Boyd. *Nonlinear Optics*. Academic Press; 2008.
- [6] A.M. Marino. Experimental studies of two-mode squeezed states in rubidium vapor. ProQuest Dissertations And Theses; Thesis (PhD)-University of Rochester, 2006; Publication Number: AAI3245848; Source: Dissertation Abstracts International, Volume: 67-12, Section: B, page: 7147; 184 p. 2006; Available from: <http://adsabs.harvard.edu/abs/2006PhDT.....226M>.
- [7] M.D. Lukin, P.R. Hemmer, M. Löffler, M.O. Scully. Resonant Enhancement of Parametric Processes via Radiative Interference and Induced Coherence.

- Physical Review Letters. 1998 Sep; 81(13):2675-2678. Available from:
<http://link.aps.org/doi/10.1103/PhysRevLett.81.2675>.
- [8] C. C. Gerry, P. L. Knight. *Introductory Quantum Optics*. Cambridge University Press, 2005.
- [9] D. Andrew, M. Babiker. (Eds.) *The Angular Momentum of Light*. 1st Edition. Cambridge University Press, 2013.
- [10] L. Carbone *et al.* (2013). The Generation of Higher-order Laguerre-Gauss Optical Beams for High-precision Interferometry. *Journal of visualized experiments : JoVE*. 10.3791/50564.
- [11] M. Vasnetsov, K. Staliunas. (Eds.) *Optical Vortices*. Horizons in World Physics; Vol. 228. Nova Science Publishers; 1999.
- [12] P. Vaity, J. Banerji, R. P. Singh, *Phys. Lett. A* 377, 1154 (2013).
- [13] M. Shutova, A. A. Zhdanova, A. V. Sokolov, Detection of mixed OAM states via vortex breakup, *Physics Letters A*, Volume 381, Issue 4, 2017, Pages 408-412, ISSN 0375-9601, <https://doi.org/10.1016/j.physleta.2016.09.031>.
- [14] S. G. Garanin, F. A. Starikov, Yu. I. Malakhov (2012). *Adaptive Optics and Optical Vortices*, *Adaptive Optics Progress*, Dr. Robert Tyson (Ed.), InTech, DOI: 10.5772/53328. Available from:
<https://mts.intechopen.com/books/adaptive-optics-progress/adaptive-optics-and-optical-vortices>
- [15] T. S. Iskhakov, I. N. Agafonov, M. V. Chekhova, G. O. Rytikov, and G. Leuchs. *Polarization properties of macroscopic Bell states*. (PRA 84, 045804, 2011)

- [16] I. Novikova *Generation of macroscopic optical polarization Bell states in atomic ensembles via four-wave mixing* . (2012)
- [17] D. Dehlinger and M. W. Mitchell. *Entangled photons, nonlocality, and Bell inequalities in the undergraduate laboratory* (Physics Department, Reed College, Portland Oregon, 2001)
- [18] H. Bauser. *Light Entanglement via Four Wave Mixing through a Rubidium Vapor Cell* (Physics Department, The College of William & Mary, Williamsburg, VA, 2016)